Corrosion behavior of a compositionally complex alloy utilizing simultaneous Al, Cr, and Ti passivation

Samuel B. Inman, Debashish Sur, Junsoo Han, Kevin Ogle, John R. Scully

To cite this version:

Samuel B. Inman, Debashish Sur, Junsoo Han, Kevin Ogle, John R. Scully. Corrosion behavior of a compositionally complex alloy utilizing simultaneous Al, Cr, and Ti passivation. Corrosion Science, 2023, 217, pp.111138. 10.1016/j.corsci.2023.111138 . hal-04051811

HAL Id: hal-04051811
https://hal.science/hal-04051811

Submitted on 25 Jun 2024

HAL is a multi-disciplinary open access archive for the deposit and dissemination of scientific research documents, whether they are published or not. The documents may come from teaching and research institutions in France or abroad, or from public or private research centers.

L'archive ouverte pluridisciplinaire **HAL**, est destinée au dépôt et à la diffusion de documents scientifiques de niveau recherche, publiés ou non, émanant des établissements d'enseignement et de recherche français ou étrangers, des laboratoires publics ou privés.

Version of Record: https://www.sciencedirect.com/science/article/pii/S0010938X23001804
Manuscript_e35b15fb21ebd66f86c8f44cb1988069

Corrosion Behavior of a Compositionally Complex Alloy Utilizing Simultaneous Al, Cr, and Ti Passivation

Samuel B. Inman[1,2], Debashish Sur[1,2], Junsoo Han[1,2,3,4], Kevin Ogle[3], John R. Scully[1,2]

[1]Department of Materials Science and Engineering, University of Virginia, 395 McCormick Road, Charlottesville, VA 22904, USA

[2]Center for Electrochemical Science and Engineering, University of Virginia, 395 McCormick Road, Charlottesville, VA 22904, USA

[3]Chimie ParisTech, PSL Research University, CNRS, Institut de Recherche Chimie Paris (IRCP), F-75005, Paris, France

[4]Sorbonne Université, Laboratoire Interfaces et Systèmes Electrochimiques, F-75005, Paris, France

Abstract

The corrosion behavior of the $Al_{0.3}Cr_{0.5}Fe_2Mn_{0.25}Mo_{0.15}Ni_{1.5}Ti_{0.3}$ compositionally complex two-phase alloy was explored in a variety of electrolytes. Comparable corrosion resistance to 316L stainless steel and Ni-Cr binaries was observed in NaCl despite lower Cr concentrations. Individual elemental fates during corrosion were identified by combinations of in-situ atomic emission spectroelectrochemistry and ex-situ X-ray photoelectron spectroscopy with high-resolution surface analysis and depth profiling. A potentiostatically grown passive film was enriched in Al(III), Cr(III), Ti(IV), and Mo(VI). Al-Ti and Cr-Ti layers were suggested but significant Al, Cr, and Ti mixing was present. Proposed benefits of Al-Cr-Ti coexistence are addressed.

© 2023 published by Elsevier. This manuscript is made available under the Elsevier user license
https://www.elsevier.com/open-access/userlicense/1.0/

Introduction

Compositionally complex alloys (CCAs), which include the high entropy alloy subclass, consist of four or more elements at concentration ranges between 5 and 35 at. % [1]. The improved compositional distribution promoted in part by a high configurational entropy enables the possibility of unique properties arising from elemental interactions not obtainable in conventional alloys [2]. Unique alloying combinations and a high degree of atomic radius mismatch give the alloy class a wide range of potentially beneficial properties including mechanical strength [2-4], thermal conductivity [5], fracture toughness [6], and high temperature behavior [7]. In addition to their role in the quest for mechanical strengthening and broad alloying flexibility, CCAs are valued for their improved combinations and distributions of corrosion resistant elements that have been suggested to improve the stability of passive films and increase resistance to aqueous corrosion [8-10]. Such strategies include consideration of solid solution oxides and long-range ordered complex oxides [10-12].

Initial CCA compositions with reliable corrosion resistance often utilized Cr concentrations at or above those conventionally seen in stainless steel (> 13 at. %) to ensure the presence of a stable protective Cr-based passive film [12-16]. To date, novel CCAs with corrosion resistance exceeding conventional alloys with similar Cr concentrations has not generally been attained [15, 17]. Computational thermodynamic modeling often predicts stable oxide miscibility and potential long-range ordered spinel formation incorporating Cr and Fe or Ni [11, 12]. However, passive films are often determined to be significantly enriched in Cr far beyond congruent oxidation tracking with the bulk composition. This suggests a disproportionate role of certain elements to attain high corrosion resistance regulated by the passive film such as Cr in the case of stainless steels, Ni-Cr based alloys, and CCAs [13, 14, 18, 19]. Enrichment is driven in part by the favorable thermodynamic stability of Cr oxides and hydroxides and selective dissolution of other elements [11, 13, 20]. Thermodynamic stability of similar passive species has been used to inform subsequent corrosion resistant CCA compositions [12, 21]. One significant opportunity in CCA design is to depart from single element passivation and explore whether combinations of elements produced desirable effects. Such combinations may promote stable passivation even when each element is below conventional critical concentrations for single passivating elements [10, 12].

Cr and Al have been long established as effective co-constituent passivating elements, mainly in Fe-Cr-Al alloys designed for high temperature oxidation and/or nuclear applications [22-27]. Notably, Springer et al. [28] demonstrated the viability of utilizing Al to reduce Cr concentrations, obtaining good corrosion resistance in salt spray testing at Cr concentrations as low as 8-10 at. %. Additionally, Hio et al. [29, 30] suggested beneficial interaction on aqueous corrosion behaviour of both Al and Si across a range of Fe-Cr alloys with Cr concentrations below 16 wt. % in sulfate and chloride containing solutions.

Recently, joint alloying of Cr and Al has been explored within corrosion resistant CCAs, often with Al introduced to decrease alloy density [31-42]. Yamanaka et al. [40] characterized the passive film of the AlCoCrFeNi CCA immersed in 3.5 wt. % NaCl, finding the film to be enriched in both Al and Cr (42.8% and 25.6% of oxidized surface features respectively). However, the detailed location of Al(III) and Cr(III) cations with regards to film layering, elemental dissolution rates, and elemental interaction were not discussed. Zhu and Zhang [43] suggested the combination of both Al or Cr to be more effective in limiting corrosion in Fe-Mn-Al-Cr alloys in sulfate and chloride solutions than the individual contributions of either element. Cr was suggested to be enriched in a inner oxide layers with Al enriched in outer layers despite the well-established solid solution solubility within the Cr_2O_3-Al_2O_3 corundum system [44]. Further characterization of Cr-Al interaction within passive films grown in aqueous conditions at room temperature is limited, unlike the well-studied oxides grown on Fe-Cr-Al alloys in high temperature systems [45-47].

While Al is well established as a passivating agent, Al additions have been tied to the formation of BCC or B2 second phase regions in the microstructure of FCC CCAs. Such heterogeneity has been tied to inferior corrosion resistance, most prominently indicated by decreased pitting potentials with increasing Al concentration [32-40]. Shi et al. [35] utilized in-situ atomic force microscopy to characterize the breakdown morphology of a series of $Al_xCoCrFeNi$ CCAs. Increasing the Al concentration over a range from 7.0 to 14.9 at. % resulted in a change in microstructure from a single-phase FCC structure to one with an FCC matrix with BCC and B2 present. Pitting potentials decreased and passive current densities increased with higher Al concentrations. Breakdown was observed to transition from random pitting in the single-phase FCC matrix to pitting at the FCC/BCC interface in the dual-phase alloys, eventually leading to preferential dissolution of the BCC phase at the maximum Al concentration. Thus, Al concentrations must be kept below thresholds governed by a given alloy's onset of a dual-phase microstructure to minimize the risk of localized corrosion.

While the behavior of Al-Cr containing CCAs has acquired some attention, Ti additions to transition metal-based CCAs also often improve corrosion resistance, largely due to the stability and protectiveness of Ti oxides [17, 48-51]. However, the miscibility and possible synergy between Ti and Al or Cr oxides in such alloys is often underexplored. Choudhary et al. [52] evaluated elemental dissolution rates and surface enrichment of a single-phase lightweight BCC AlCrTiV CCA. Oxides from all four constituent elements were present in the passive film with significant Al_2O_3 enrichment (38.8% of surface cation fractions after immersion at OCP as opposed to 12.4%, 19.9%, and 12.9% in the case of Cr, Ti, and V, respectively). Cr and V depletion in the passive film was tied to incongruent transpassive dissolution observed during polarization. Qiu et al. [53] evaluated the $Al_{1.5}CrTiV$ CCA with similar methods, observing significant Al oxide presence within the passive film formed in chloride solution with Cr and Ti passivation also observed despite high dissolution rates. In both cases, the stability of a four-oxide passive film was hypothesized to promote the wide passive range observed during polarization, demonstrating the viability of Al, Cr, and Ti interaction in the design of corrosion-resistant CCAs. However, the high Cr and Ti concentrations may limit the studies' viability for low-cost CCA design, where Cr and Ti concentrations are decreased and interactions with additional elements are of concern. Thus, establishing enrichment relations between Al, Cr, and Ti possibly altered by additional transition metals (e.g., Fe, Ni) that often dominate CCA compositions remains an important issue in the design of CCAs with reduced concentrations of traditional passivating elements.

Despite benefiting corrosion resistance and decreasing alloy density, Ti concentrations in transition metal CCAs are constrained by the persistent concern of second phase formation at high Ti concentrations, often of BCC or B2 structure [1, 54-57]. In some cases, such second phase formation leads to susceptibility to localized corrosion and decreased pitting potentials brought about by the addition of Al and/or Ti [56, 57]. Such risks to localized corrosion constrain the concentrations of Al or Ti that may be added to FCC CCAs, eliminating the possibility of complete reliance on either element to passivate. Localized corrosion may be further resisted by alloying with other minor elements such as Mo [58].

The use of Al, Cr and Ti as joint passivating elements has the potential to reduce density of corrosion resistant alloys for lightweight applications while also introducing new elements with well-established passivation ability. However, elemental partitioning during second phase formation and localized corrosion requires further attention. Understanding the role of Al and Ti in second phase formation will help to establish effective compositional bounds within CCA design and allows for selection of passivating elements without detrimental phase formation.

Additionally, the presence of three passivators, raises questions regarding the nature of the oxide formed during passivation. Possible oxide natures include: (i) oxide layering, (ii) phase separation of stoichiometric single element oxides within the passive film, (iii) an oxide solid solution, (iv) a new complex oxide, (v) a combination of the above descriptions. The addition of other passivating elements may enable passivation below traditional Cr thresholds. For example, Mo has a long-established contribution to corrosion resistance [59, 60] and has been found to operate in the passive film [61, 62]. This benefit that has recently been extended to CCA design [8]. Mo generally increases the corrosion resistance across a wide range of CCA compositions [63, 64]. Potential mechanisms include inhibition of dissolution reactions [65, 66], contributions towards stability and/or protectiveness of oxide films, particularly those dominated by Cr(III), [61], and doping of Cr_2O_3 oxides to induce a favorable cation vacancy interaction [62]. The well-established synergy also leads to Cr enrichment within the passive films of Ni-Cr-Mo alloys [61]. However, little work has been done evaluate the effect of Mo on other stable passivators utilized in CCAs such as Al and Ti.

Increased Mo concentration has been suggested to induce and stabilize second phase formation in CCA microstructures. The affinity of Cr to Mo often leads to the formation of sigma or mu phases which can deplete the remaining microstructure from both elements [58, 63, 64, 67]. The addition of Mo to Al [67] and Ti-containing [68] CCAs has similarly induced second phase formation, however, unlike with Cr, Mo preferentially partitions away from Al and Ti. Therefore, the effect of Mo on corrosion may deviate from conventional wisdom and can not be forecast from simplified binary or tertiary systems. In this study Mo was also included at fixed low concentration.

This work describes the synthesis and corrosion properties of a novel dual-phase FCC CCA using the strategy of simultaneous Al, Cr, and Ti passivity at low concentrations of each element. The combined benefits of the three elements and contributions to corrosion resistance are evaluated. In subsequent work, individual contributions of the matrix and second phases will be evaluated separately to determine the contributions of microstructure and elemental partitioning. In this study, passivation and breakdown leading to local corrosion were evaluated with global AC and DC electrochemical methods in a variety of environments. Tracking of dissolution and passive film enrichment evaluates the fate of each constituent element. Impedance-based and surface sensitive chemical characterization of the passive film formed during air exposure, open circuit corrosion, and within the passive range provide insight into film growth and implications for stability. The results are compared to a stainless steel and Ni-Cr binary alloys to check for any unique effects not seen in conventional alloys that often occur in compositionally complex alloys

[2, 10]. The resulting passivity of the alloy validates the combined benefits of combinations of low concentrations of Al, Cr, and Ti below traditional critical thresholds in binary alloys and provides a foundation for the design of future lightweight corrosion resistant CCAs.

Methods

Alloy Selection and Sample Preparation

A lightweight low-cost CCA of the nominal composition $Al_{0.3}Cr_{0.5}Fe_2Mn_{0.25}Mo_{0.15}Ni_{1.5}Ti_{0.3}$ (henceforth referred to as LC-CCA) was synthesized via arc melting high purity elements (Cr purity > 99.2%, all other metals purity > 99.9%) in an argon atmosphere and flipped five times to ensure homogeneity. Buttons approximately 1 cm in diameter were suction cast into a water-cooled copper mold. Compositions were selected to include lightweight passivating elements (e.g., Al, Ti) to target passivity below traditional Cr concentrations utilized in initial CCAs such as CoCrFeMnNi (20 at. %) and commercially produced corrosion resistant alloys such as 316L (17.1-19.2 at. %) with methodology discussed further elsewhere [69]. Table I compares the LC-CCA composition to experimental controls used throughout the study: three pure constituent elements, two binary Ni-Cr alloys intended to match the LC-CCA Cr and total passivating element (Al, Cr, and Ti) concentration, and commercially produced (North American Steel) 316L. Ni-Cr alloys were arc melted and annealed to promote single-phase FCC microstructure with method described further elsewhere [14]. Traditional Austenitic stabilizers were utilized in the LC-CCA to preserve an FCC microstructure including Ni and Mn, for which the concentration was optimized for corrosion resistance in the alloy system in prior work [70]. Notably, Co is not included due to the high cost and density with low-cost Fe, Mn, and Al prioritized instead.

The LC-CCA was encapsulated in quartz tubing under Ar and annealed at 1070 °C for 5 hours before quenching in water, a treatment suggested to promote a dual-phase FCC + $L2_1$ microstructure by both computational thermodynamic modeling (Thermocalc 2019b, TCHEA3 database [71]) and machine learning methods discussed elsewhere [72, 73]. Samples were ground with silica carbide paper to a 1200 grit finish, and degreased with an organic solvent before microstructural (with samples polished to a 0.25-micron finish with diamond suspension) and electrochemical evaluation. Phase and surface morphology was observed via scanning electron microscopy (SEM) on a FEI Quanta 650 system in back scattered electron (BSE) mode both prior to and following extended aqueous exposure. Phase compositions were quantified with energy dispersive spectroscopy (EDS) point scans and maps analyzed with Oxford Instruments AZtec software [74].

Electrochemical Characterization of Corrosion Behavior

The corrosion resistance and passive film stability were initially evaluated with two extended immersion tests at room temperature: 20 day immersion in a 0.1 M NaCl solution adjusted to pH 4 with 1.0 M HCl and 72 hour immersion in approximately 6.0 wt. % $FeCl_3$ as defined by ASTM G-48-A [75] modified to utilize the smaller button samples (1 cm diameter and 0.3 cm thickness) and a 316L sample of similar dimensions. Pitted surfaces were imaged with the SEM setup described above following immersion.

A Gamry Instrument Reference 600+ potentiostat and conventional three electrode cell with the LC-CCA (approximately 0.875 cm^2 exposed area) as the working electrode, a platinum mesh counter electrode, and a saturated calomel reference electrode (SCE, 0.241 V vs. standard hydrogen electrode) were used for AC and DC electrochemical corrosion experimentation. Passivation and breakdown characterization was initially evaluated in dilute NaCl at natural pH (approximately 5.75) and H_2SO_4 (pH 1) to ensure an observable passivation process. The samples were exposed in 0.01 M NaCl to a potentiostatic treatment of -1.3 V_{SCE} (V vs. SCE) for 600 s intended to minimize air-formed oxides before cyclic polarization from -1.3 to 0.8 V_{SCE} at a scan rate of 0.5 mV/s. For pure Al, Cr, and Ti, the cathodic applied potential step initial polarization potential was decreased to -2.25 V_{SCE}, (-1.75 V_{SCE} for Mn), to promote complete reduction of the air-formed oxides. Impedance was monitored in-situ at a frequency of 1 Hz and an applied AC voltage of 20 mV_{rms}, as the imaginary component has been previously utilized to track film thickness[1] [18, 76]. The LC-CCA was also polarized in additional electrolytes prepared with NaCl concentrations of 1.0 M, 0.1 M, and 0.001 M. Polarization in 0.01 M NaCl with the pH adjusted to 2 and 4 with 1.0 M HCl and to 6, 8, 10, and 12 with 1.0 M NaOH was also evaluated and is shown in the supplementary information section. All electrolyte solutions were continually bubbled with $N_{2(g)}$ to reduce the activity of dissolved oxygen. Polarization (bypassing impedance measurements) was also evaluated for the LC-CCA in solutions containing 0.1 M H_2SO_4 and NaCl at concentrations of 0.01, 0.1, and 1.0 M. Polarization experiments were repeated three times to ensure reproducibility.

Specific elemental dissolution rates were tracked during polarization in 0.1 M NaCl adjusted to pH 4 and 10, where the pH and NaCl concentration was adjusted relative to initial polarization evaluation described above to increase dissolution rates beyond detection limits, with an inductively coupled plasma atomic emission spectroelectrochemistry (AESEC) apparatus (Horiba Jobin Yvon Ultima) described elsewhere [77]. A polychromator with focal length of 0.5 m and a monochromator with focal length of 1.0 m were used to detect elements dissolved in the electrolyte. For the pH 4 solution, Mo signal was obtained by the monochromator and for the pH 10 solution, Al signal was obtained by the monochromator improve the resolution of each element. Emission intensities at characteristic wavelengths for each element were used to calculate equivalent dissolution current densities using Faraday's law with methods described in the supplementary information section and elaborated further elsewhere [77]. The $N_{2(g)}$ bubbling, and in-situ impedance monitoring used in the polarization procedure described above were bypassed during AESEC experimentation. AESEC was also used to obtain elemental dissolution rates during potentiostatic

---

[1] The previously utilized direct proportionality between in-situ impedance measurements and passive film thickness depends on film properties including the dielectric constant and constant phase element behavior as well as parallel plate capacitor assumptions. Such properties are expected to change with film composition and morphology during growth procedures. Therefore, any in-situ impedance measurements are limited to qualitative representations of film thickness trends and are not intended to yield exact thickness.

holds at -0.2 V_{SCE} following a -1.3 V_{SCE} cathodic treatment for 600 s and utilizing the same electrolyte solutions and AESEC setup described above. Results are available in the supplementary information section.

The passive film formed on the LC-CCA under three different conditions were further characterized with potentiostatic electrochemical impedance spectroscopy (EIS) in 0.01 M NaCl under $N_{2(g)}$ bubbling. To characterize the air-formed film, the LC-CCA was exposed to open circuit potential for 30 minutes directly after mechanical grinding before obtaining a full EIS spectrum ranging from 100 kHz to 1 mHz at the stable OCP (5 points/decade, 20 mV_{rms}).

To evaluate the effect of extended aqueous exposure at OCP on the air-formed oxide, the procedure above was repeated, however, the exposure period was extended to 40 ks before EIS at the final OCP. Each film was compared to a passive film grown from a reduced surface in aqueous environments previously evaluated [70] using a third procedure. The air-formed oxide was first minimized using the -1.3 V_{SCE} exposure described above. The surface was then exposed to a potentiostatic hold for 40 ks at -0.25 V_{SCE}, a potential determined to be within the LC-CCA passive range from initial polarization. Impedance was monitored in-situ during film growth (1 Hz, 20 mV_{rms}) and was followed by a full EIS spectrum described above with the DC potential maintained at -0.25 V_{SCE}.

X-ray Photoelectron Spectroscopy Characterization of Passive Film

The surface film composition and valence states were transported under $N_{2(g)}$ and evaluated with a PHI VersaProbe III X-ray photoelectron spectroscopy (XPS) system following the EIS procedure for extended OCP exposure and -0.25 V_{SCE} exposure. The air-formed oxide film was evaluated directly after mechanical grinding with no electrolyte exposure. XPS spectra were acquired and with Al Kα X-rays (1,468.7 eV) at a 26 eV pass energy, 0.05 eV step size, and 45° take off angle over a 100 µm by 100 µm spot size. High-resolution spectra over the O 1s, Al 2p, Cr $2p_{3/2}$, Fe $2p_{1/2}$[2], Mn $2p_{1/2}$[2], Mo 3d, Ni $2p_{3/2}$, and Ti 2p series were collected, calibrated to the C 1s series (284.8 eV), and deconvoluted with KOLXPD analysis software [78]. Intensities were normalized with relative sensitivity factors obtained via PHI Multipak [79]. Spectra were fit to the following features: Shirley background substitutions, Doniach-Sunjic peaks for metallic features, and Voigt functions for oxidized features, to known reference compounds based off position, peak intensity, width, and multiplet splitting [80-83]. The film grown at -0.25 V_{SCE} was further characterized with depth profiling. The film was sputtered with Ar over a 3 mm by 3 mm area at 1 keV for 7 minutes with sweeps over each constituent element core series taken at 15 second intervals (112 eV pass energy, 0.2 eV step size, 100 µm square spot size, 45° take-off angle). The intensities over both metallic and oxidized region of the spectrum were normalized with relative sensitivity factors to evaluate trends in oxide layering.

Results

Alloy Microstructure

Figure 1 shows the microstructure and mapping of the elemental distribution of the homogenized (1070° C, 5 hours) LC-CCA. The microstructure consisted of a matrix phase and second phase regions with sizes on the order of single microns. The second phase area fraction was determined to be 4.33% via BSE imaging and crystal structures were identified as FCC and Heusler ($L2_1$) by X-ray diffraction in previous work [70], confirming computational predictions [70, 72]. The FCC matrix was enriched in Fe, Cr, and Mo, while the $L2_1$ phase was enriched in Al, Ni, and Ti. However, each element was present in both phases. Mn was relatively uniformly distributed between both phases. The composition of each phase previously obtained [70] via EDS is tabulated in the supplementary information section.

---

[2] The Fe $2p_{1/2}$ and Mn $2p_{1/2}$ series were utilized as opposed to the higher intensity $2p_{3/2}$ series due to overlap with Ni Auger peaks. A constant position shift for all features was assumed relative to the known feature positions from references for each elements' $2p_{3/2}$ spectra.

Behavior in H_2SO_4 and Evaluation of Passivation in a Cl^- Free Environment

Evaluation of corrosion resistance in H_2SO_4 focusses on the active to passive transition, dissolution, and passivity in an environment where only key passivating elements may operate as opposed to localized breakdown [32, 76]. When polarized in 0.1 M H_2SO_4, the LC-CCA exhibited superior passivation ability to both Ni-Cr binary samples and comparable behavior to 316L, as shown in Figure 2. The LC-CCA had a similar corrosion potential (E_{Corr}) to Ni-20Cr and 316L during upward polarization. Both the LC-CCA and 316L showed a significantly lower critical or primary passivation current density than both Ni-Cr binaries, suggesting more efficient and potentially more rapid passivation from the perspective of the h factor, i.e., the number of monolayers of metallic alloy dissolved to form an infinitely connected passive film during the stage of primary passivation [84]. Furthermore, the passive current density (i_{Pass}) was of similar magnitude to 316L and lower than both Ni-Cr binaries, suggesting the formation of an improved passive film. Transpassive dissolution and oxygen evolution were observed for all alloys slightly above 0 V_{SCE}. This behaviour may indicate a strong presence of Cr(III) within the passive film at lower potentials that enables a subsequent potential-dependent change in valence state (e.g. Cr(III) to Cr(VI)) [85] whilst the exclusive presence of Al(III) and Ti(IV) [86] oxides would preclude this possibility. Moreover, the oxygen evolution reaction is often observed to be slow on thick insulating oxides of Al and Ti [87-89]. Despite the lower Cr concentrations in the LC-CCA (10 at. %) than Ni-20Cr and 316L (roughly 18 at. %), the transpassive dissolution potential (E_{Trans}) and dissolution rates were similar for all alloys, establishing the potential for improved passivity without following the conventional strategy of increasing Cr content above a critical threshold.

Behavior in NaCl and Localized Breakdown Characterization

The significant effects of Cl^- ions on passivation behavior and localized passive film breakdown were addressed by exposure to NaCl solutions of varying concentrations. Passivation of the LC-CCA over all NaCl concentrations is suggested by Figure 3. i_{Pass} was less than 10^{-5} A.cm^{-2} in 0.5 mV/sec upward scans and did not show a clear trend correlating with NaCl concentration. The imaginary component of impedance (-Z”) at 1 Hz, a proportional indicator to passive film thickness, increased in magnitude almost linearly with respect to potential in the passive range (~-0.5 - 0.5 V_{SCE}). Low -Z” at -1.3 V_{SCE} suggest near-complete reduction of the air-formed oxide film during the cathodic treatment prior to polarization. -Z” decreased at potentials at or near the pitting potential (E_{Pit}), suggesting growth and breakdown of the passive film. E_{Pit} decreased from 0.623 to 0.030 V_{SCE} with increasing NaCl concentration from 0.001 to 1 M. Sharp spikes slightly at potentials below E_{Pit} in the current density and -Z” are most visible in the 0.001 and 0.01 M conditions, suggesting initiation of metastable pits that repassivated prior to stabilization. Stable pitting at potentials above E_{Pit} was indicated by a sharp increase in the current density. Pits were visible on the sample surfaces polarized in all four NaCl concentrations following exposure with no apparent pattern with regards to overall sample geometry. However, they were generally larger and more frequent following testing in more concentrated NaCl solutions. A positive hysteresis was present in all four NaCl concentrations and the repassivation potential (E_{Rep}) decreased with NaCl concentration (Figure S.2).

The addition of NaCl to 0.1 M H_2SO_4 shown in Figure 4 showed little effect on E_{Corr} or i_{Pass}. A negative hysteresis was present in unadjusted H_2SO_4 and H_2SO_4 with 0.01 M NaCl. The hysteresis transitioned to positive in the 0.1 M and 1.0 M NaCl added H_2SO_4 solutions, suggesting a transition from transpassive dissolution to pitting breakdown. Pitting in more NaCl concentrated solution, most noticeably in the case of 1.0 M NaCl added H_2SO_4 solution, was further indicated by spikes in the current density and a value of E_{Pit} below E_{Trans} observed in dilute solutions.

The passivation and breakdown of the LC-CCA does not mirror any of the constituent single elements, as shown by the polarization data in 0.01 M NaCl compared to pure Al, Cr, and Ti in Figure 5. For instance, E_{Corr} was below that of Ti and well above that of Cr and Al. i_{Pass} of the LC-CCA was comparable to Al and slightly lower than Cr, but was well above that of Ti. The maximum LC-CCA -Z” was comparable to Cr and below that of Al and Ti. E_{Pit} was below that of Cr and Ti, whose films did not completely break down within the evaluation range, but well above the Al E_{Pit} near -0.4 V_{SCE}. The characteristic passivation parameters were also not readily estimated by averages of constituent elements. This is regulated by the nature of the elemental interplay within the oxide film which is not likely to follow property averaging based off the bulk alloy composition.

The polarization behavior of the LC-CCA in 0.01 M NaCl is compared to 316L and both Ni-Cr binaries as shown in Figure 6 and summarized in Table II. The LC-CCA showed the most positive E_{Pit}, suggesting improved passive film resistance to breakdown. Given that the LC-CCA has a lower Cr content (10 at. %) than Ni-20Cr and 316L (~18.3 at. %), it is suggested that the replacement of Cr with Al and Ti have some contribution that maintains and potentially improves passive film protectiveness and pit stabilization tendency. Passivation may include formation independent metal oxides or synergistic behavior with between the three elements as discussed below.

AESEC was utilized to obtain the elemental dissolution current densities in 0.1 M NaCl pH 4 and pH 10 during potentiodynamic polarization as shown in Figure 7. No dissolution was observed in either pH below E_{Pit}. Al rates are not shown in Figure 7 a due to low signal with respect to noise, however, the lack of detection is indicative of relatively low Al dissolution rates in the passive region which, similar to Cr and Ti, suggests stability and presence in the passive film. Beyond E_{Pit}, dissolution occurs at higher rates with Fe and Ni dissolving at the highest ratios with the dissolution rates approaching tranpassive dissolution at near-stoichiometric ratios at high potentials. Further analysis of elemental dissolution rates obtained via AESEC including dissolution observed during potentiostatic holds as well as LC-CCA polarization behavior across a range of pH are available in the supplementary information section.

Passive Film Impedance and Cation Fractions

During the 40 ks exposure of the LC-CCA under open circuit condition with no initial cathodic treatment and an initially unaltered air-formed oxide, OCP rose from -0.262 to -0.155 V_{SCE} (Figure S.4), potentially indicating a decreased driving force for dissolution. The OCP of measured after film growth at -0.25 V_{SCE} reached a stable value of -0.042 V_{SCE} (not shown), higher than that any value observed during open circuit condition exposure of the air-formed oxide for the same time duration.

EIS characterization of the air-formed, OCP exposed, and passive range exposed films is shown in Figure 8 and fit to an equivalent circuit model (ECM) modified from Jakupi et al. [90] (Figure 8 e) with parameters listed in Table III. All three evaluated LC-CCA films showed polarization resistance (R_P), defined as the total non-solution resistive components in the ECM, above 10^5 Ω.cm^2, suggesting good resistance to corrosion. As the resistance attributed to the film was multiple orders of magnitude higher than the resistance attributed to the film-electrolyte interface for all fitted spectra, R_P trends closely follow the film resistance values (R_f). The R_P value for the film grown in the passive region from an initially cathodically polarized substrate is nearly doubled that of the air-formed oxide. The extended exposure of the air-formed oxide at OCP has little effect on R_P or the constant phase element coefficients (α), as values were similar to those of the initial air-formed oxide. Figures 8 c and 8 d compare the EIS spectra of the film grown electrochemically on the LC-CCA at -0.25 V_{SCE} to films grown on the Ni-Cr binaries and 316L under the same conditions. Similar to the in-situ impedance measured during polarization, the Ni-Cr binaries had higher impedance moduli in the low frequency domain. In the Bode plots, all the curves showed a reasonably constant phase frequency domain (0.1-10 Hz) where α values associated with the film were near or above 0.8 (~ -72°). Alternatively, the parameters associated with the film/electrolyte interface generally have lower α values and resistances. The impedance modulus follows fairly linear behavior with frequency in between flat regions at high and low frequencies characteristic of the R_S and R_P respectively. Current density and in-situ -Z” measurements are shown in the supplementary information.

The chemical composition and oxidation states of the air-formed, OCP exposed, and electrochemically grown films and relevant XPS deconvolutions are reported in Table IV and Figure 9 respectively[3]. Passive films grown under all conditions reported here were enriched in Cr and Ti relative to the bulk composition. The air-formed oxide and electrochemically grown oxide were also enriched in Al, while Mo was present in the air-formed and OCP exposed films. Films grown under all three conditions were depleted in Fe, Ni, and Mn relative to bulk compositions. The cation fractions of Al, Fe, and Mn in the film decreased during the 40 ks OCP exposure relative to the air-formed oxide, potentially suggesting preferential dissolution. Alternatively, Cr, Mo, and Ni cation fractions increased, although the relative enrichment may arise from the preferential dissolution of Al, Fe, and Mn as opposed to preferential passivation during exposure. Unlike the oxide grown electrochemically at -0.25 V_{SCE}, OCP exposure did not cause any significant increase in Ti cation fraction relative to the air-formed oxide.

The surface of the electrochemically grown film (-0.25 V_{SCE}, 40 ks) was dominated by Ti with a suggested surface cation percentage of 55.4%. The film was also enriched in Al and Cr. XPS analysis suggested the film contains TiO_2 and $Cr(OH)_3$ with limited signal attributed to Cr_2O_3 and $FeCr_2O_4$. The Al signal could not be further deconvoluted beyond metallic features, oxidized features, and the Cr 3s spectra that overlapped the region. Thus, all oxidized features were fit as a single Al_2O_3 peak.

Oxide and hydroxide peak fitting results suggest Cr(III) exists in a variety of molecular conditions. Significant Cr hydroxylation is suggested to occur during 40 ks OCP exposure based upon the dominant $Cr(OH)_3$ peak formed whereas the air-formed oxide peak was fit to Cr_2O_3. Additionally, the fitting results indicate $FeCr_2O_4$ and $NiCr_2O_4$ presence, potentially suggesting preferential interaction of Fe and Ni cations

---

[3] It is of note that the XPS spot size was significantly larger than the areas of individual $L2_1$ regions, thus the surface characterization was assumed to be a homogenous representation of the film grown over both phases. The possibility of microstructural partitioning on film enrichment forms the basis for future work that will isolate the passive film grown over each phase and evaluate film homogeneity of the dual-phase material.

with Cr, although the low intensity and possibility of solid solution oxides make it difficult to confirm the presence of a long-range ordered spinel species.

XPS sputter depth profiling shown in Figure 10 revealed local enrichment of Al, Cr, and Ti at roughly similar depths within the passive film electrochemically grown in 0.01 M NaCl at -0.25 V_{SCE}. To isolate the signal attributable to oxidized features and evaluate potential oxide layering, the intensities of each element within the binding energy regions associated with oxidized features and metallic features are identified separately. Generally lower intensities of both metallic and oxidized features at low sputtering time are attributed to carbon surface contamination. The highest levels of Mo and Fe in an oxidized state can be observed at shorter sputtering times (or shallow depths) than the highest Al, Cr, and Ti, suggesting outer layer enrichment. However, even within the Mo and Fe enriched outer regions, the film is still dominated by Al, Cr, and Ti. The highest intensities of Ti, Al, and Cr oxides are all observed near 1.25 minutes of sputtering and each elements' depth profile followed similar trends with sputtering times, suggesting some miscibility between Al, Cr, and Ti within the passive film or co-location within the XPS penetration depth. The metal intensities increase with increased sputtering time and generally approach the bulk metal composition at extended sputtering depths while carbon and oxygen become lower or disappear. It is of note that depth profiling suggests higher intensities of Cr throughout most of the passive film than Ti with the notable exception of the surface. Thus, although the surface, which governs key electrochemical reactions may be dominated by Ti, it is possible that the interior regions of the film may have more Cr than suggested by the high-resolution scans. Although the depth profiling provides accurate assessment of potential layering, it is of note that quantitative assessment of oxidized features may be limited, particularly past three minutes of sputtering where the oxygen signal is below half of the maximum signal. It should be further noted that no structural information is provided by XPS and reference to molecules is uncertain.

Immersion Mass Loss Evaluation

Table V shows mass loss data for the air-formed oxides of the LC-CCA and 316L obtained during the ASTM G-48-A test (~6 wt. % $FeCl_3$, 25°C) and extended immersion in 0.1 M NaCl pH 4. The pH adjustment was utilized due to previous inconclusive results in unadjusted 0.1 M NaCl, where neither sample had observable mass loss [70]. The $FeCl_3$ exposure yielded mass loss rates for the LC-CCA which were approximately 150% higher than those of 316 L and well above rates observed in NaCl. Pits on the size order of hundreds of microns were observed with no magnification on both alloys and can be seen in Figure S.6. Pits on the LC-CCA were generally larger and more frequent than those on 316L. For both alloys, pits were more frequent near the edges of the sample. Some corrosion product was visible near the pits before cleaning and no corrosion product was visible on the non-pitted regions of the surface. In 0.1 M NaCl pH 4, the LC-CCA had a significantly higher mass loss rate (5.994 $mg.cm^{-2}.y^{-1}$) than 316L (0.833 $mg.cm^{-2}.y^{-1}$), and generally had more stable pits form. Non-spherical pits were disproportionately observed at or near the second phase interface, however, the $L2_1$ phase was not observed to be preferentially dissolved. This lack of preferential dissolution of either phase indicates the interface may serve as a preferential pit initiation site, a phenomenon further suggested by frequent pitting observed at the interface such as in the case of Figure S.6 e.

Discussion

Thermodynamic Factors Influencing Passive Film Formation

Thermodynamic influences played a strong role in passive film composition. Elements enriched in the passive film shown in Table VI generally from stable oxides (e.g., TiO_2, Cr_2O_3, Al_2O_3) indicated by favorable Gibbs free energies of formation [91, 92] and broad stability ranges on E-pH diagrams [86]. All films were enriched in Ti, Cr, and, with the exception of the oxide exposed to OCP, Al with enrichment and depletion quantified by the ratio of cation fractions in the passive film suggested by XPS to the bulk alloy composition in atomic percent. Al, Cr, and Ti were all enriched relative to alloy composition in the passive film grown at -0.25 V_{SCE} over 40 ks with Ti suggested to be the dominant species at the surface of the passive film (Table IV) by high-resolution XPS spectra (Figure 9). The Ti(IV) appears to exceed the concentrations needed to form a continuous protective TiO_2 layer [93], although there is no defined threshold as is the case in the Fe-Cr system. Kim et al. [94] passivated three Fe-Ti binary alloys with Ti concentrations of 38, 57, and 77 at. % at 1 V_{SHE} in 5 M HCl. Ti formed the majority of the passive film for each alloy. Both the Ti surface cation fraction and the overall corrosion resistance increased with bulk Ti fraction, however the lack of evaluation below 38 at. % makes comparison of critical Ti thresholds between the LC-CCA and Fe-Ti systems impractical.

The higher local surface enrichment ratio of Ti compared to Al and Cr could possibly be rationalized by the favorable free energy of formation of TiO_2 (-959.1 kJ/mol [91]) relative to Al_2O_3 (-1690.7 kJ/mol [91]) and Cr_2O_3 (-1050.0 kJ/mol [92]) on a per cation basis, which may be relevant in the comparatively oxygen rich environment near the surface (Figure 10 b), despite not being preferred on a molecular level. Cr_2O_3 and Al_2O_3 exhibit solid solution solubility [44] in each other. In contrast, the solid solution solubility of both Al_2O_3 [95] and Cr_2O_3 [96] is limited with TiO_2, which does not possess the corundum crystal structure. Furthermore, both Ti_2CrO_5 and $TiAl_2O_5$ have similar enthalpies of formation (within 0.3 eV/atom) as disordered solid solution oxides of the same respective compositions, as illustrated by the convex-hull diagrams in Figure 11 [97]. This potentially leaves open the possibility of stability of these complex oxides, however, convex-hull plots do not account for entropic contributions that may further stabilize solid solution oxides and decrease the likelihood of complex oxide ordering. XPS data analysis suggested the presence of stoichiometric Al and Ti oxides, although the limited availability of reference spectra such as core level binding energies for complex Ti oxides limits any possibility of phase identification via XPS. Fe was depleted in the evaluated passive films. Fe_2O_3 has been suggested to be miscible with Cr_2O_3 and $FeCr_2O_4$ has been suggested to be stable in some CCA passive films [11]. However, the strong depletion of Fe in the LC-CCA passive film grown within the passive region (Table VI) limits the possibility of significant stoichiometric $FeCr_2O_4$ presence despite the high thermodynamic stability (-1339.40 kJ/mol [92]) as there is insufficient Fe(II) in the oxide to accommodate the Cr(III) an observation confirmed by the XPS spectral data analysis (Figure 9).

Although computational methods such as CALPHAD have demonstrated the ability to account for both solid solution solubility and structure in a Ni-Cr-Fe-Mn-Co CCA oxide passive films [11], such work has not been extended to explore Al-Cr-Ti mixing. Given that Al and Cr were not suggested to form separate oxide layers from Ti by depth profiling results, it is likely that the enthalpy of mixing contribution for the respective oxides did not initiate a significant barrier to miscibility. It could be speculated that a combination of cations within the passive film may allow enhanced corrosion resistance relative to any individual element oxide and yielded strong corrosion resistance given lower alloyed Al and Cr concentrations than the traditional 12-13 at. % threshold seen in Fe-Cr based alloys [98] and the 15 at. % concentration necessary for formation of a stable passive film on Fe-Al alloys binary alloys in H_2SO_4 electrolyte [87]. The suggested layering indicates that complete miscibility between the three elements was not observed, and thus, further investigation regarding the morphological and structural nature of the oxide is required.

E-pH diagrams for the pure metals and oxides of constituent elements are often uses as guidelines for oxide stability. However, the viability of such predictions is limited as such diagrams do not account for interactions between multiple cations that were suggested by the sputter depth profiling (Figure 10 b) nor interfacial energies present between phases separated oxides. Furthermore, two elements may form a long-ranged ordered oxide such as a spinel that has stability aided by ordering contributions to the enthalpy of formation. In addition to the complex Al, Cr, and Ti containing oxides that are suggested to potentially be stable by Figure 11, Fe-Cr and Ni-Cr spinel species have also been experimentally verified to form during passivation of similar CCAs [13, 76]. Such interactions may account for deviations from behavior that would otherwise be observed for pure metals, for example those illustrated by the CALPHAD-guided E-pH diagrams produced for the $Ni_{38}Fe_{20}Cr_{22}Mn_{10}Co_{10}$ [11].

Kinetic Factors Influencing Passivation

Passive film enrichment or selective depletion has been independently suggested to be predicted from the ratio of solute element dissolution rates compare to the solvent elements by Kirchheim et al. [19] and directly measured elemental dissolution rates in an alloy via AESEC by Ogle et al. [77]. The experimentally observed surface cation fractions are compared to values predicted from pure element current densities at -0.25 V_{SCE} and equivalent dissolution rates normalized by the valence of the most likely dissolved species with methods modified from Kirchheim et al. [19] (Table VI). For instance, i_{Pass} is lower for Ti than Al. Thus, Al can be expected to dissolve at higher rates in the passive region leaving Ti to be enriched in the passive film. A more detailed methodology may be found in the supplementary information section.

In both cases, the dissolution rates are normalized to that of a dominant element (Fe in the case of the LC-CCA) with decreased dissolution rates relative to the matrix assumed to correspond to passivating species remaining in the passive film while Fe is assumed to completely dissolve. Therefore, the low dissolution and release rates of solubilized Al, Cr, and Ti observed via AESEC are consistent with the enrichment in the passive film suggested by i_{Pass} of each element and observed via XPS (Table VI), likely indicating a role in the oxides identities seen. The passive film composition calculated during potentiostatic oxide growth in the passive range, which show progressive Al, Cr, and Ti enrichment with increasing time (Figure S.7), and calculation methodology are further elaborated within the supplementary information section. However, quantitative analysis is limited by dissolution rates of Al, Cr, Mo, and Ti at or below the respective AESEC detection limits during passive dissolution, particularly during exposure to potentials within the passive region. Calculation from dissolution rates (Table VI) correctly predicted the Cr and Ti enrichment. Ni dissolved at low rates in the pure metal state and was thus predicted to be enriched in the passive film. However, metallic Ni XPS signal was only slightly enriched near the metal-oxide interface and there was little Ni oxide signal throughout the whole film, suggesting little contribution to passivation (Figure 10). Excess Al is predicted at the surface when calculating from elemental dissolution rates using AESEC (Figure S.7). Such dissolution rates are affected by the presence Cr and/or Ti cations in the passive film, which may promote the stability of Al cations. However, the high passive current density of pure Al as a single element (Figure 5) without such interactions leads to prediction of depletion via Kirchheim's method (Table VI).

Passive Film Protectiveness

A multi-cation film may be a result of thermodynamic stability but this is not necessarily the same attribute or feature that controls passivation kinetics nor protectiveness against breakdown in Cl^- containing environments. Passivation kinetics are regulated by either surface of the ionic crystal or other defect properties including formation energy and mobility [42, 99]. Cation miscibility within the passive film, particularly when the dopant cation has a lower valence state, has been shown to decrease the oxygen anion vacancy formation energy in both Al-doped TiO_2 [100] and Ni-doped Cr_2O_3 [101]. Lower oxygen anion vacancy formation energies would promote an increased oxygen vacancy concentration. This brings about a corresponding increase in electron charge carriers to maintain charge neutrality. Relative to the oxide films of 316L, Ni-10Cr, and Ni-20Cr that are dominated by undoped Cr, this could create a more reactive oxide from a kinetic standpoint. An increased oxygen vacancy concentration may increase the governing film formation reaction rates for films formed involving oxygen vacancy diffusion [102], and may therefore justify the higher i_{pass} values observed during polarization of the LC-CCA in NaCl (Figure 6). Alternatively, the increased i_{pass} may arise from the Al cation fraction, as Al_2O_3 dominated passive films are generally more porous than those dominated by Cr_2O_3 [9, 37]. i_{pass} of the LC-CCA was of similar magnitude to pure Al, while the Cr and/or Ni dominated passive films present in the Ni-Cr binaries and 316L had lower i_{pass} values (Figures 5, 6). This effect was not observed during polarization in H_2SO_4 (Figure 2), potentially due to the acidic environment reducing the presence of Al in the LC-CCA passive film by dissolving it rapidly to form Al^{3+}. Effects of vacancy formation that may increase i_{Pass} are not suggested to play a negative role in the breakdown process given the increased pitting potential of the LC-CCA relative to the Ni-Cr binaries. It is often believed that these defects do not regulate pit initiation, however, the formation of cation vacancy clusters may [103]. Other favorable attributes which enhance corrosion protection such as Cl^- adsorption, incorporation, or morphological roughening are unknown.

Enriched Elements and Film Electrochemistry at Extended Times

Extended oxide aging, either through exposure to open circuit potential or a fixed applied potential has the ability to alter the chemistry, structure and defective nature of the passive film and, by extension, the protectiveness or resistance to corrosion. Conventional wisdom generally suggests thermodynamic stable oxides with high driving forces may prevail at long times [104]. Complete reliance on accelerated corrosion testing such as potentiodynamic polarization and/or characterization of air-formed oxide chemistry limits the assessment of performance during extended aqueous exposure.

Of the LC-CCA three passive films evaluated, the film grown at -0.25 V_{SCE} had the highest R_P, suggesting the best resistance to corrosion in the unadjusted 0.01 M NaCl (Table III). The improved resistance to corrosion may be aided by the high levels of Ti within the passive film and corresponding high thermodynamic stability. Exposure to a potential within the passive range provides driving force for enrichment in thermodynamically favorable passive films. This phenomenon has been illustrated by Wang et al. [105] in CoCrFeMnNi. Application of a potential in the passive range led to the formation of a passive film more enriched in Cr, the cation that was most thermodynamically favorable, oxide relative to air-formed and OCP exposed passive films. Similar trends were observed with the increasing thermodynamically favorable Ti enrichment at the surface of the LC-CCA film grown in the passive range.

The air-formed film exposed to OCP for 40 ks had a R_P similar to that of the air-formed oxide. This oxide was alternatively enriched in Cr by exposure ageing, with Ti concentration being maintained at similar levels to the air-formed oxide. This may suggest Ti enrichment in the film was most critical in improving R_P, either through independent additive contributions or synergistic attributes with Al or Cr. Mo was enriched in the film exposed to OCP (Table VI) and outer layer of the film formed during exposure to the passive range (Figure 10). This enrichment, in conjunction with increasing Mo dissolution rates in the active region during polarization (Figure 7), may suggest that Mo plays a role in the repassivation process similar to the Ni-Cr-Mo system [106]. However, the effects of Mo on the proposed Al-Cr-Ti synergy remain unexplored.

Conclusions

A low-cost dual-phase CCA with corrosion resistance dependent on simultaneous Al, Cr, and Ti passivation below any binary alloy threshold was synthesized and evaluated utilizing a combination of electrochemical and surface characterization techniques. The following conclusions were observed and may be implemented for future Al and Ti containing CCA reiterations:

- Corrosion resistance was similar to that of 316L as indicated by a slightly improved pitting potential and similar passive current densities in a dilute NaCl solution. The use of Al and Ti at low concentrations (5-10 at. %) is validated in corrosion resistant CCA design to reduce density and ensure corrosion resistance below critical Cr concentration thresholds seen in Fe-Cr based alloys.
- The passive films were found to be enriched in Ti, Cr, and often Al. Significant Ti enrichment not seen in the air-formed oxide was observed in the passive film grown during extended exposure to a potential in the passive region. Ti was suggested to be miscible with Cr and Al from both sputter depth profiling and from thermodynamic calculations, forming solid solution oxides. Miscibility

with Ti and/or other cations may have improved the stability of Al in the passive film at potentials beyond the stability region of oxide formed on pure Al.

- The corrosion resistance was superior to single-phase FCC alloys with similar concentrations of passivating elements. Non-stochiometric dissolution and passivation were observed suggesting neither phase was vulnerable to preferential dissolution despite pitting being observed at the phase interface.

Acknowledgments

This work was supported by the United States Office of Naval Research award # N00014-19-1-2420 under the directorship of Dave Shifler. K. Ogle and AESEC experimentation were supported by Agence Nationale de Recherche, award # ANR-20-CE08-0031 (Tapas 2020). Characterization equipment including the PHI VersaProbe III and Quanta 650 SEM was provided by the UVA Nanomaterials Characterization Facility (NMCF). The PHI VersaProbe III was supported by NSF award # 162601. Stephen McDonnell contributed to XPS analysis. Peter Connors developed the convex hull diagrams. Jie Qi and Diego Ibarra Hoyos assisted with sample synthesis under the guidance of S. Joseph Poon. Mark A. Wischhusen assisted with EDS analysis under the guidance of Sean R. Agnew.

References

[1] R. Feng, C. Lee, M. Mathes, T.T. Zuo, S. Chen, J. Hawk, Y. Zhang, P. Liaw, Design of Light-Weight High-Entropy Alloys, Entropy, 18 (2016) 333.

[2] D.B. Miracle, O.N. Senkov, A critical review of high entropy alloys and related concepts, Acta Materialia, 122 (2017) 448-511.

[3] M.-H. Tsai, J.-W. Yeh, High-Entropy Alloys: A Critical Review, Materials Research Letters, 2 (2014) 107-123.

[4] W. Li, D. Xie, D. Li, Y. Zhang, Y. Gao, P.K. Liaw, Mechanical behavior of high-entropy alloys, Progress in Materials Science, 118 (2021) 100777.

[5] M.-H. Tsai, Physical Properties of High Entropy Alloys, in: Entropy, 2013, pp. 5338-5345.

[6] B. Gludovatz, A. Hohenwarter, D. Catoor, E.H. Chang, E.P. George, R.O. Ritchie, A fracture-resistant high-entropy alloy for cryogenic applications, Science, 345 (2014) 1153-1158.

[7] J. Chen, X. Zhou, W. Wang, B. Liu, Y. Lv, W. Yang, D. Xu, Y. Liu, A review on fundamental of high entropy alloys with promising high–temperature properties, Journal of Alloys and Compounds, 760 (2018) 15-30.

[8] Y. Qiu, S. Thomas, M.A. Gibson, H.L. Fraser, N. Birbilis, Corrosion of high entropy alloys, npj Materials Degradation, 1 (2017) 15.

[9] Y. Shi, B. Yang, P.K. Liaw, Corrosion-Resistant High-Entropy Alloys: A Review, Metals, 7 (2017) 43.

[10] J.R. Scully, S.B. Inman, A.Y. Gerard, C.D. Taylor, W. Windl, D.K. Schreiber, P. Lu, J.E. Saal, G.S. Frankel, Controlling the corrosion resistance of multi-principal element alloys, Scripta Materialia, 188 (2020) 96-101.

[11] K. Wang, J. Han, A.Y. Gerard, J.R. Scully, B.-C. Zhou, Potential-pH diagrams considering complex oxide solution phases for understanding aqueous corrosion of multi-principal element alloys, npj Materials Degradation, 4 (2020) 35.

[12] C.D. Taylor, P. Lu, J. Saal, G.S. Frankel, J.R. Scully, Integrated computational materials engineering of corrosion resistant alloys, npj Materials Degradation, 2 (2018) 6.

[13] A.Y. Gerard, J. Han, S.J. McDonnell, K. Ogle, E.J. Kautz, D.K. Schreiber, P. Lu, J.E. Saal, G.S. Frankel, J.R. Scully, Aqueous passivation of multi-principal element alloy Ni38Fe20Cr22Mn10Co10: Unexpected high Cr enrichment within the passive film, Acta Materialia, 198 (2020) 121-133.

[14] A.Y. Gerard, E.J. Kautz, D.K. Schreiber, J. Han, S. McDonnell, K. Ogle, P. Lu, J.E. Saal, G.S. Frankel, J.R. Scully, The Role of Chromium Content on Aqueous Passivation of Non-Equiatomic Ni38Fe20CrxMn21-0.5xCo21-0.5x Multi-Principal Element Alloy (x = 22, 14, 10, 6 at. %) in Acidic Chloride Solution, Acta Materialia, (2022) 118607.

[15] H. Luo, Z. Li, A.M. Mingers, D. Raabe, Corrosion behavior of an equiatomic CoCrFeMnNi high-entropy alloy compared with 304 stainless steel in sulfuric acid solution, Corrosion Science, 134 (2018) 131-139.

[16] A. Rodriguez, J.H. Tylczak, M. Ziomek-Moroz, Corrosion Behavior of CoCrFeMnNi High-Entropy Alloys (HEAs) Under Aqueous Acidic Conditions, ECS Transactions, 77 (2017) 741-752.

[17] Y. Qiu, M.A. Gibson, H.L. Fraser, N. Birbilis, Corrosion characteristics of high entropy alloys, Materials Science and Technology, 31 (2015) 1235-1243.

[18] K. Lutton, K. Gusieva, N. Ott, N. Birbilis, J.R. Scully, Understanding multi-element alloy passivation in acidic solutions using operando methods, Electrochemistry Communications, 80 (2017) 44-47.

[19] R. Kirchheim, B. Heine, H. Fischmeister, S. Hofmann, H. Knote, U. Stolz, The passivity of iron-chromium alloys, Corrosion Science, 29 (1989) 899-917.

[20] J. Han, X. Li, A.Y. Gerard, P. Lu, J.E. Saal, G.S. Frankel, K. Ogle, J.R. Scully, Potential Dependent Mn Oxidation and Its Role in Passivation of Ni38Fe20Cr22Mn10Co10 Multi-Principal Element Alloy Using

Multi-Element Resolved Atomic Emission Spectroelectrochemistry, Journal of The Electrochemical Society, 168 (2021) 051508.

[21] P. Lu, J.E. Saal, G.B. Olson, T. Li, O.J. Swanson, G.S. Frankel, A.Y. Gerard, K.F. Quiambao, J.R. Scully, Computational materials design of a corrosion resistant high entropy alloy for harsh environments, Scripta Materialia, 153 (2018) 19-22.

[22] Z. Duan, H. Yang, Y. Satoh, K. Murakami, S. Kano, Z. Zhao, J. Shen, H. Abe, Current status of materials development of nuclear fuel cladding tubes for light water reactors, Nuclear Engineering and Design, 316 (2017) 131-150.

[23] K.G. Field, M.A. Snead, Y. Yamamoto, K.A. Terrani, Handbook on the Material Properties of FeCrAl Alloys for Nuclear Power Production Applications, in, US Department of Energy, 2017.

[24] K.A. Gamble, T. Barani, D. Pizzocri, J.D. Hales, K.A. Terrani, G. Pastore, An investigation of FeCrAl cladding behavior under normal operating and loss of coolant conditions, Journal of Nuclear Materials, 491 (2017) 55-66.

[25] D.J. Park, H.G. Kim, J.Y. Park, Y.I. Jung, J.H. Park, Y.H. Koo, A study of the oxidation of FeCrAl alloy in pressurized water and high-temperature steam environment, Corrosion Science, 94 (2015) 459-465.

[26] R. Rebak, K. Terrani, W. Gassmann, J. Williams, K. Ledford, Improving Nuclear Power Plant Safety with FeCrAl Alloy Fuel Cladding, MRS Advances, (2017) 1-8.

[27] I.M. Wolff, L.E. Iorio, T. Rumpf, P.V.T. Scheers, J.H. Potgieter, Oxidation and corrosion behaviour of Fe–Cr and Fe–Cr–Al alloys with minor alloying additions, Materials Science and Engineering: A, 241 (1998) 264-276.

[28] H. Springer, C. Baron, L. Tanure, M. Rohwerder, A combinatorial study of the effect of Al and Cr additions on the mechanical, physical and corrosion properties of Fe, Materials Today Communications, 29 (2021) 102947.

[29] K. Hio, T. Adachi, T. Yamada, Y. Tsuchida, K. Nakajima, Y. Hosoi, Effects of Al, Si and Mo on Passivation Characteristics of Fe-10Cr Alloys, MATERIALS TRANSACTIONS, 42 (2001) 1723-1730.

[30] K. Hio, T. Yamada, Y. Tsuchida, K. Nakajima, Y. Hosoi, Effect of Chromium Content on Anodic Polarization Characteristics of Fe-Cr-Al and Fe-Cr-Si Alloys, Corrosion, 58 (2002) 124-131.

[31] S. Choudhary, N. Birbilis, S. Thomas, Evolution of Passivity for the Multi-Principal Element Alloy CoCrFeNi with Potential, pH and Exposure in Chloride Solution, Corrosion, (2021).

[32] Y.-F. Kao, T.-D. Lee, S.-K. Chen, Y.-S. Chang, Electrochemical passive properties of AlxCoCrFeNi (x=0, 0.25, 0.50, 1.00) alloys in sulfuric acids, Corrosion Science, 52 (2010) 1026-1034.

[33] C.P. Lee, C.C. Chang, Y.Y. Chen, J.W. Yeh, H.C. Shih, Effect of the aluminium content of AlxCrFe1.5MnNi0.5 high-entropy alloys on the corrosion behaviour in aqueous environments, Corrosion Science, 50 (2008) 2053-2060.

[34] B.-y. Li, K. Peng, A.-p. Hu, L.-p. Zhou, J.-j. Zhu, D.-y. Li, Structure and properties of FeCoNiCrCu0.5Alx high-entropy alloy, Transactions of Nonferrous Metals Society of China, 23 (2013) 735-741.

[35] Y. Shi, L. Collins, N. Balke, P.K. Liaw, B. Yang, In-situ electrochemical-AFM study of localized corrosion of AlxCoCrFeNi high-entropy alloys in chloride solution, Applied Surface Science, 439 (2018) 533-544.

[36] Y. Shi, L. Collins, R. Feng, C. Zhang, N. Balke, P.K. Liaw, B. Yang, Homogenization of AlxCoCrFeNi high-entropy alloys with improved corrosion resistance, Corrosion Science, 133 (2018) 120-131.

[37] Y. Shi, B. Yang, X. Xie, J. Brechtl, K.A. Dahmen, P.K. Liaw, Corrosion of AlxCoCrFeNi high-entropy alloys: Al-content and potential scan-rate dependent pitting behavior, Corrosion Science, 119 (2017) 33-45.

[38] C.-C. Yen, H.-N. Lu, M.-H. Tsai, B.-W. Wu, Y.-C. Lo, C.-C. Wang, S.-Y. Chang, S.-K. Yen, Corrosion mechanism of annealed equiatomic AlCoCrFeNi tri-phase high-entropy alloy in 0.5 M H2SO4 aerated aqueous solution, Corrosion Science, 157 (2019) 462-471.

[39] P. Cui, Z. Bao, Y. Liu, F. Zhou, Z. Lai, Y. Zhou, J. Zhu, Corrosion behavior and mechanism of dual phase Fe1.125Ni1.06CrAl high entropy alloy, Corrosion Science, 201 (2022) 110276.

[40] K. Yamanaka, H. Shiratori, M. Mori, K. Omura, T. Fujieda, K. Kuwabara, A. Chiba, Corrosion mechanism of an equimolar AlCoCrFeNi high-entropy alloy additively manufactured by electron beam melting, npj Materials Degradation, 4 (2020) 24.

[41] E.M. Godlewska, M. Mitoraj-Królikowska, J. Czerski, M. Jawańska, S. Gein, U. Hecht, Corrosion of Al(Co)CrFeNi High-Entropy Alloys, Frontiers in Materials, 7 (2020).

[42] Y. Qiu, S. Thomas, R.K. Gupta, T. Gengenbach, R. Jones, N. Birbilis, A Surface Study of the Native Oxide upon a Compositionally Complex Alloy, Corrosion, 74 (2018) 1312-1317.

[43] X.M. Zhu, Y.S. Zhang, Investigation of the Electrochemical Corrosion Behavior and Passive Film for Fe-Mn, Fe-Mn-Al, and Fe-Mn-Al-Cr Alloys in Aqueous Solutions, Corrosion, 54 (1998) 3-12.

[44] P. Zhao, H. Zhao, J. Yu, H. Zhang, H. Gao, Q. Chen, Crystal structure and properties of Al2O3-Cr2O3 solid solutions with different Cr2O3 contents, Ceramics International, 44 (2018) 1356-1361.

[45] C. Wagner, Passivity and inhibition during the oxidation of metals at elevated temperatures, Corrosion Science, 5 (1965) 751-764.

[46] F.H. Stott, G.C. Wood, J. Stringer, The influence of alloying elements on the development and maintenance of protective scales, Oxidation of Metals, 44 (1995) 113-145.

[47] E. Airiskallio, E. Nurmi, M.H. Heinonen, I.J. Väyrynen, K. Kokko, M. Ropo, M.P.J. Punkkinen, H. Pitkänen, M. Alatalo, J. Kollár, B. Johansson, L. Vitos, Third element effect in the surface zone of Fe-Cr-Al alloys, Physical Review B, 81 (2010) 033105.

[48] R.K. Mishra, P.P. Sahay, R.R. Shahi, Alloying, magnetic and corrosion behavior of AlCrFeMnNiTi high entropy alloy, Journal of Materials Science, 54 (2019) 4433-4443.

[49] X.W. Qiu, Y.P. Zhang, C.G. Liu, Effect of Ti content on structure and properties of Al2CrFeNiCoCuTix high-entropy alloy coatings, Journal of Alloys and Compounds, 585 (2014) 282-286.

[50] M. Wu, R.C. Setiawan, D.Y. Li, Benefits of passive element Ti to the resistance of AlCrFeCoNi high-entropy alloy to corrosion and corrosive wear, Wear, 492-493 (2022) 204231.

[51] W. Guo, J. Li, M. Qi, Y. Xu, H.R. Ezatpour, Effects of heat treatment on the microstructure, mechanical properties and corrosion resistance of AlCoCrFeNiTi0.5 high-entropy alloy, Journal of Alloys and Compounds, 884 (2021) 161026.

[52] S. Choudhary, Y. Qiu, S. Thomas, N. Birbilis, Element-resolved electrochemical analysis of transpassive dissolution and repassivation behavior of the multi-principal element alloy AlTiVCr, Electrochimica Acta, 362 (2020) 137104.

[53] Y. Qiu, R. Liu, T. Gengenbach, O. Gharbi, S. Choudhary, S. Thomas, H.L. Fraser, N. Birbilis, Real-time dissolution of a compositionally complex alloy using inline ICP and correlation with XPS, npj Materials Degradation, 4 (2020) 7.

[54] S. Gao, T. Kong, M. Zhang, X. Chen, Y.W. Sui, Y.J. Ren, J.Q. Qi, F.X. Wei, Y.Z. He, Q.K. Meng, Z. Sun, Effects of titanium addition on microstructure and mechanical properties of CrFeNiTix (x = 0.2–0.6) compositionally complex alloys, Journal of Materials Research, 34 (2019) 819-828.

[55] Z. Tang, L. Huang, W. He, P.K. Liaw, Alloying and Processing Effects on the Aqueous Corrosion Behavior of High-Entropy Alloys, Entropy, 16 (2014) 895-911.

[56] W. Qi, W. Wang, X. Yang, G. Zhang, W. Ye, Y. Su, Y. Li, S. Chen, Effects of Al and Ti co-doping on the strength-ductility- corrosion resistance of CoCrFeNi-AlTi high-entropy alloys, Journal of Alloys and Compounds, 925 (2022) 166751.

[57] D.H. Xiao, P.F. Zhou, W.Q. Wu, H.Y. Diao, M.C. Gao, M. Song, P.K. Liaw, Microstructure, mechanical and corrosion behaviors of AlCoCuFeNi-(Cr,Ti) high entropy alloys, Materials & Design, 116 (2017) 438-447.

[58] Y.L. Chou, J.W. Yeh, H.C. Shih, The effect of molybdenum on the corrosion behaviour of the high-entropy alloys Co1.5CrFeNi1.5Ti0.5Mox in aqueous environments, Corrosion Science, 52 (2010) 2571-2581.

[59] K. Sugimoto, Y. Sawada, The role of molybdenum additions to austenitic stainless steels in the inhibition of pitting in acid chloride solutions, Corrosion Science, 17 (1977) 425-445.

[60] M. Klimmeck, A study of the kinetics of passive layer formation on Cr-Mo alloys, Electrochimica Acta, 25 (1980) 1375-1381.

[61] K. Lutton Cwalina, C.R. Demarest, A.Y. Gerard, J.R. Scully, Revisiting the effects of molybdenum and tungsten alloying on corrosion behavior of nickel-chromium alloys in aqueous corrosion, Current Opinion in Solid State and Materials Science, 23 (2019) 129-141.

[62] G. Tranchida, F. Di Franco, M. Santamaria, Role of Molybdenum on the Electronic Properties of Passive Films on Stainless Steels, Journal of The Electrochemical Society, 167 (2020) 061506.

[63] X.-L. Shang, W. Zhijun, Q. Wu, J.-C. Wang, J.-J. Li, J.-K. Yu, Effect of Mo Addition on Corrosion Behavior of High-Entropy Alloys CoCrFeNiMox in Aqueous Environments, Acta Metallurgica Sinica (English Letters), 32 (2018).

[64] Z. Niu, Y. Wang, C. Geng, J. Xu, Y. Wang, Microstructural evolution, mechanical and corrosion behaviors of as-annealed CoCrFeNiMox (x = 0, 0.2, 0.5, 0.8, 1) high entropy alloys, Journal of Alloys and Compounds, 820 (2020) 153273.

[65] R.C. Newman, The dissolution and passivation kinetics of stainless alloys containing molybdenum—1. Coulometric studies of Fe-Cr and Fe-Cr-Mo alloys, Corrosion Science, 25 (1985) 331-339.

[66] R.C. Newman, The dissolution and passivation kinetics of stainless alloys containing molybdenum—II. Dissolution kinetics in artificial pits, Corrosion Science, 25 (1985) 341-350.

[67] J.M. Zhu, H.M. Fu, H.F. Zhang, A.M. Wang, H. Li, Z.Q. Hu, Microstructures and compressive properties of multicomponent AlCoCrFeNiMox alloys, Materials Science and Engineering: A, 527 (2010) 6975-6979.

[68] Y.L. Chou, J.-W. Yeh, H.C. Shih, The effect of molybdenum on the corrosion behaviour of the high-entropy alloys Co1.5CrFeNi1.5Ti0.5Mox in aqueous environments, Corrosion Science, 52 (2010) 2571-2581.

[69] J.J. Bhattacharyya, S.B. Inman, M.A. Wischhusen, J. Qi, J. Poon, J.R. Scully, S.R. Agnew, Light Weight, Low Cost, and Compositionally Complex Multiphase Alloys with Optimized Strength, Ductility and Corrosion Resistance: Discovery, Design and Mechanistic Understandings, Submitted to Materials & Design, (2023).

[70] S.B. Inman, J. Han, A.Y. Gerard, J. Qi, M.A. Wischhusen, S.R. Agnew, S.J. Poon, K. Ogle, J.R. Scully, Effect of Mn Content on the Passivation and Corrosion of Al0.3Cr0.5Fe2MnxMo0.15Ni1.5Ti0.3 Compositionally Complex Face-Centered Cubic Alloys, Corrosion, 78 (2021) 32-48.

[71] J.O. Andersson, T. Helander, L. Höglund, P.F. Shi, B. Sundman, Thermo-Calc and DICTRA, Computational tools for materials science, in, 2002.

[72] J. Qi, A.M. Cheung, S.J. Poon, High Entropy Alloys Mined From Binary Phase Diagrams, Scientific Reports, 9 (2019) 15501.

[73] J. Qi, A.M. Cheung, S.J. Poon, Navigating the Complex Compositional Landscape of High-Entropy Alloys, 2021.

[74] O. Instruments, AZtec, in.

[75] ASTM G48-11: Standard Test Methods for Pitting and Crevice Corrosion Resistance of Stainless Steels and Related Alloys by Use of Ferric Chloride Solution, (2020).

[76] K.F. Quiambao, S.J. McDonnell, D.K. Schreiber, A.Y. Gerard, K.M. Freedy, P. Lu, J.E. Saal, G.S. Frankel, J.R. Scully, Passivation of a corrosion resistant high entropy alloy in non-oxidizing sulfate solutions, Acta Materialia, 164 (2019) 362-376.

[77] K. Ogle, Atomic Emission Spectroelectrochemistry: Real-Time Rate Measurements of Dissolution, Corrosion, and Passivation, Corrosion, 75 (2019) 1398-1419.

[78] J. Libra, KolXPD, in.

[79] Ulvac-Phi, MultiPak, in, 2017.

[80] M.C. Biesinger, L.W.M. Lau, A.R. Gerson, R.S.C. Smart, Resolving surface chemical states in XPS analysis of first row transition metals, oxides and hydroxides: Sc, Ti, V, Cu and Zn, Applied Surface Science, 257 (2010) 887-898.

[81] M.C. Biesinger, B.P. Payne, A.P. Grosvenor, L.W.M. Lau, A.R. Gerson, R.S.C. Smart, Resolving surface chemical states in XPS analysis of first row transition metals, oxides and hydroxides: Cr, Mn, Fe, Co and Ni, Applied Surface Science, 257 (2011) 2717-2730.

[82] J. Baltrusaitis, B. Mendoza-Sanchez, V. Fernandez, R. Veenstra, N. Dukstiene, A. Roberts, N. Fairley, Generalized molybdenum oxide surface chemical state XPS determination via informed amorphous sample model, Applied Surface Science, 326 (2015) 151-161.

[83] A. Obrosov, R. Gulyaev, A. Zak, M. Ratzke, M. Naveed, W. Dudzinski, S. Weiß, Chemical and Morphological Characterization of Magnetron Sputtered at Different Bias Voltages Cr-Al-C Coatings, Materials, 10 (2017) 156.

[84] K. Sieradzki, R.C. Newman, A percolation model for passivation in stainless steels, J. Electrochem. Soc.; (United States), 133:9 (1986) Medium: X; Size: Pages: 1979-1980.

[85] T.P. Moffat, R.M. Latanision, An Electrochemical and X-Ray Photoelectron Spectroscopy Study of the Passive State of Chromium, Journal of The Electrochemical Society, 139 (1992) 1869.

[86] M. Pourbaix, Atlas of electrochemical equilibria in aqueous solutions, (1974).

[87] J. Peng, F. Moszner, J. Rechmann, D. Vogel, M. Palm, M. Rohwerder, Influence of Al content and pre-oxidation on the aqueous corrosion resistance of binary Fe-Al alloys in sulphuric acid, Corrosion Science, 149 (2019) 123-132.

[88] P.J. Boddy, Oxygen Evolution on Semiconducting TiO2, Journal of The Electrochemical Society, 115 (1968) 199.

[89] A.G. Scheuermann, J.D. Prange, M. Gunji, C.E.D. Chidsey, P.C. McIntyre, Effects of catalyst material and atomic layer deposited TiO2 oxide thickness on the water oxidation performance of metal–insulator–silicon anodes, Energy & Environmental Science, 6 (2013) 2487-2496.

[90] P. Jakupi, D. Zagidulin, J.J. Noël, D.W. Shoesmith, The impedance properties of the oxide film on the Ni–Cr–Mo Alloy-22 in neutral concentrated sodium chloride solution, Electrochimica Acta, 56 (2011) 6251-6259.

[91] J.D. Cox, D.D. Wagman, V.A. Medvedev, CODATA key values for thermodynamics, New York, 1984.

[92] S.E. Ziemniak, L.M. Anovitz, R.A. Castelli, W.D. Porter, Thermodynamics of Cr2O3, FeCr2O4, ZnCr2O4, and CoCr2O4, The Journal of Chemical Thermodynamics, 39 (2007) 1474-1492.

[93] D. Schlain, J.S. Smatko, Passivity of Titanium in Hydrochloric Acid Solutions, Journal of The Electrochemical Society, 99 (1952) 417.

[94] H. Kim, N. Akao, N. Hara, K. Sugimoto, Comparison of Corrosion Resistances Between Fe2O3 - TiO2 Artificial Passivation Film and Passivation Film on Fe-Ti Alloy, Journal of The Electrochemical Society, 145 (1998) 2818.

[95] S.M. Lang, C.M. Fillmore, L.H. Maxwell, The System Beryllia-Alumina-Titania: Phase Relations and General Physical Properties of Three Component Porcelains, Journal of Research of the National Bureau of Standards 48 (1952) 298-312.

[96] S. Sōmiya, S. Hirano, S. Kamiya, Phase relations of the Cr2O3-TiO2 system, Journal of Solid State Chemistry, 25 (1978) 273-284.

[97] A. Jain, S.P. Ong, G. Hautier, W. Chen, W.D. Richards, S. Dacek, S. Cholia, D. Gunter, D. Skinner, G. Ceder, K.A. Persson, Commentary: The Materials Project: A materials genome approach to accelerating materials innovation, APL Materials, 1 (2013) 011002.

[98] H.H. Uhlig, G.E. Woodside, Anodic Polarization of Passive and Non-passive Chromium–Iron Alloys, The Journal of Physical Chemistry, 57 (1953) 280-283.

[99] C.B. Nascimento, U. Donatus, C.T. Ríos, R.A. Antunes, Electronic properties of the passive films formed on CoCrFeNi and CoCrFeNiAl high entropy alloys in sodium chloride solution, Journal of Materials Research and Technology, 9 (2020) 13879-13892.

[100] A. Iwaszuk, M. Nolan, Charge compensation in trivalent cation doped bulk rutile TiO2, Journal of Physics: Condensed Matter, 23 (2011) 334207.

[101] J.J. Carey, M. Legesse, M. Nolan, Low Valence Cation Doping of Bulk Cr2O3: Charge Compensation and Oxygen Vacancy Formation, The Journal of Physical Chemistry C, 120 (2016) 19160-19174.

[102] B. Roh, D. Macdonald, Effect of oxygen vacancies in anodic titanium oxide films on the kinetics of the oxygen electrode reaction, Russian Journal of Electrochemistry, 43 (2007) 125-135.

[103] D.D. Macdonald, The Point Defect Model for the Passive State, Journal of The Electrochemical Society, 139 (1992) 3434.

[104] L.N. Walters, E.L. Wang, J.M. Rondinelli, Thermodynamic Descriptors to Predict Oxide Formation in Aqueous Solutions, The Journal of Physical Chemistry Letters, 13 (2022) 6236-6243.

[105] L. Wang, D. Mercier, S. Zanna, A. Seyeux, M. Laurent-Brocq, L. Perrière, I. Guillot, P. Marcus, Study of the surface oxides and corrosion behaviour of an equiatomic CoCrFeMnNi high entropy alloy by XPS and ToF-SIMS, Corrosion Science, 167 (2020) 108507.

[106] X. Li, K. Ogle, The Passivation of Ni-Cr-Mo Alloys: Time Resolved Enrichment and Dissolution of Cr and Mo during Passive-Active Cycles, Journal of The Electrochemical Society, 166 (2019) C3179-C3185.

Figure and Table Captions

Table I: LC-CCA, Ni-Cr, and 316L nominal compositions in atomic percent. 316L compositions are defined as the median of the commercial supplier composition range

Figure 1: a) BSE micrograph of LC-CCA microstructure and b) EDS mapping of LC-CCA second-phase region. Figure 1 b was reproduced from [61]

Figure 2: Potentiodynamic polarization of LC-CCA, Ni-Cr binaries, and 316L in $N_{2(g)}$ bubbled 0.1 M H_2SO_4 following cathodic reduction pre-treatment (600 s, -1.3 V_{SCE})

Figure 3: a) Potentiodynamic polarization and b) in-situ imaginary impedance (1 Hz) measurement of LC-CCA in $N_{2(g)}$ bubbled NaCl solutions of varying concentration at a neutral pH (5.5-6) following cathodic reduction pre-treatment (600 s, -1.3 V_{SCE})

Figure 4: Upward (solid) and reverse (dashed) potentiodynamic polarization of LC-CCA in $N_{2(g)}$ bubbled 0.1 M H_2SO_4 with varying concentrations of NaCl following cathodic reduction pre-treatment (600 s, -1.3 V_{SCE})

Figure 5: a) Potentiodynamic polarization and b) in-situ imaginary impedance (1 Hz) of LC-CCA and pure constituent passivating elements in $N_{2(g)}$ bubbled 0.01 M NaCl (pH ~5.75) following cathodic reduction pre-treatment at a potential dependent on the constituent element standard half-cell potential

Figure 6: a) Potentiodynamic polarization and b) in-situ imaginary impedance (1 Hz) of LC-CCA, Ni-Cr binaries, and 316L in $N_{2(g)}$ bubbled 0.01 M NaCl (pH ~5.75) following cathodic reduction pre-treatment (600 s, -1.3 V_{SCE})

Table II: Selected corrosion parameters from potentiodynamic polarization shown in Figure 5 a. Each term includes the average value with a one standard deviation bound

Figure 7: Equivalent current densities of in-situ elemental dissolution rates monitored via AESEC during upward polarization of the LC-CCA in 0.1 M NaCl a) pH 4 and b) pH 10. Equivalent current densities are determined from the elemental flow rates with equation S.2

Figure 8: a) Bode and b) Nyquist plots of the EIS spectra for the passive films grown during air-exposure, extended OCP exposure, and extended potentiatic exposure (-0.25 V_{SCE}) following cathodic reduction pre-treatment (600 s, -1.3 V_{SCE}). Additionally, c) Bode and d) Nyquist plots compare EIS spectra of the LC-CCA film formed during extended potentiatiostatic exposure with films grown on Ni-Cr binaries and 316L. All films were characterized in $N_{2(g)}$ bubbled 0.01 M NaCl (pH~5.75) and e) ECM diagram

Table III: EIS circuit fit parameters for the spectra indicated in Figure 7. CPE components include an admittance (Y) and CPE coefficient (α). The Warburg component (W) consists of an admittance (Y) term and a finite length bound coefficient (B)

Figure 9: XPS spectra and fits for key passivating elements in films grown on the LC-CCA during air-exposure, extended OCP exposure ($N_{2(g)}$ bubbled 0.01 M NaCl), and extended potentiatic exposure ($N_{2(g)}$ bubbled 0.01 M NaCl, -0.25 V_{SCE}, cathodic reduction pre-treatment)

Table IV: Surface cation fractions obtained from XPS fits indicated in Figure 7

Table V: Mass loss rates for the LC-CCA and 316 L compared with previously obtained data in 0.1 M NaCl (pH~5.75) [61]

Figure 10: XPS sputter depth profiles showing cumulative intensities of peaks fit to a) metallic features and b) oxidized features for each element

Table VI: XPS enrichment factors calculated with a modified model from Kirchheim et al. (equations S.5-S.6) compared with enrichment factors calculated via experimental XPS surface cation fractions (equation S.7)

Figure 11: Convex-Hull diagrams for the a) Cr-Ti-O and b) Al-Ti-O systems indicating the formation enthalpy of potentially compounds obtained via Materials Project [82].

Figure 1

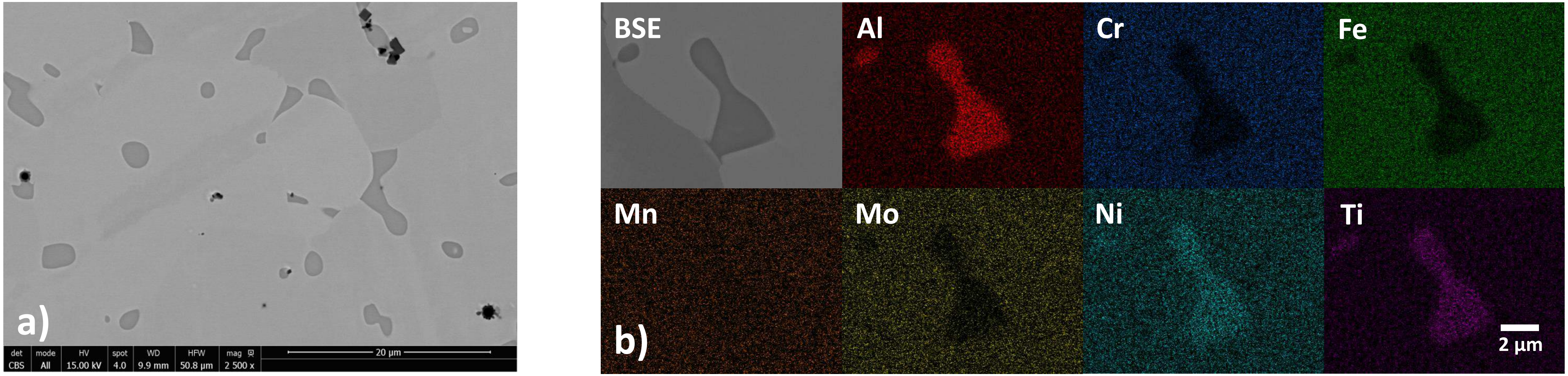
a)
det
CBS
mode
All
HV
15.00 kV
spot
4.0
WD
9.9 mm
HFW
50.8 µm
mag
2 500 x
20 µm
b)
BSE
Al
Cr
Fe
Mn
Mo
Ni
Ti
2 µm

Figure 2

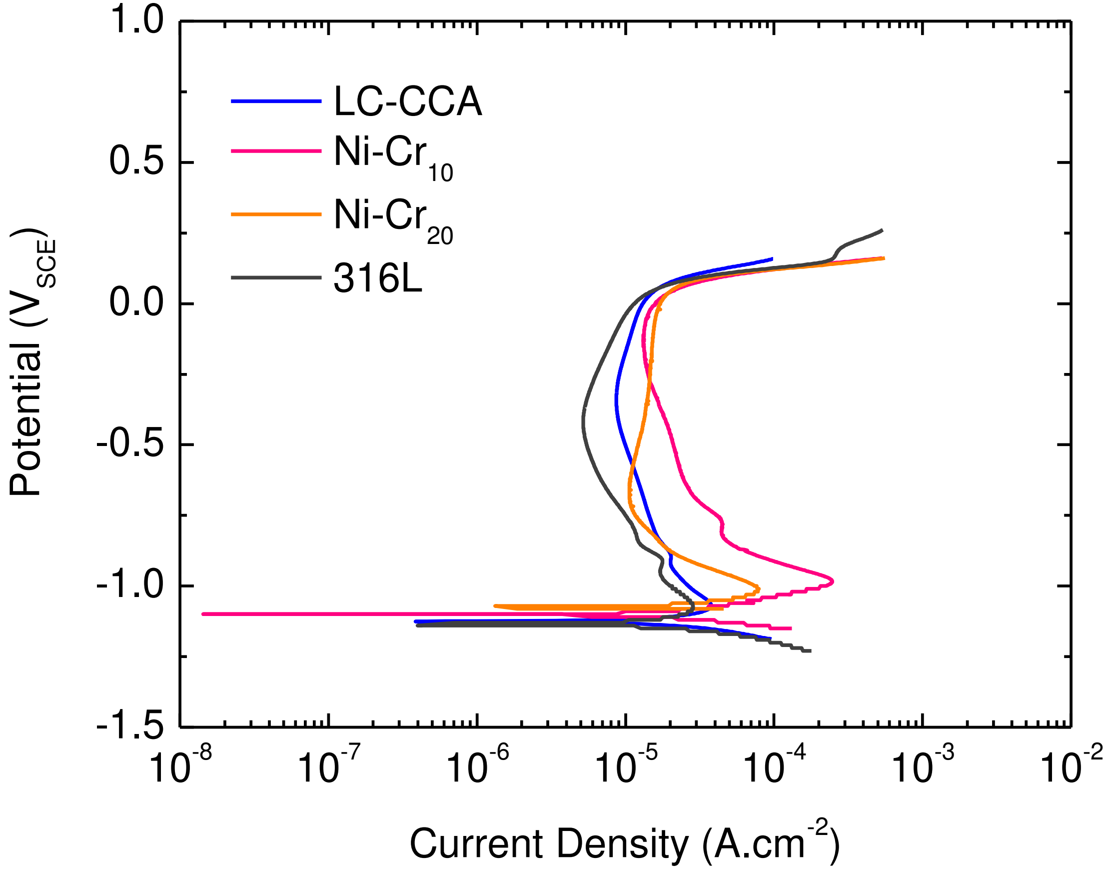

LC-CCA
Ni-Cr$_{10}$
Ni-Cr$_{20}$
316L
Potential (V$_{SCE}$)
1.0
0.5
0.0
-0.5
-1.0
-1.5
10^{-8}
10^{-7}
10^{-6}
10^{-5}
10^{-4}
10^{-3}
10^{-2}
Current Density (A.cm^{-2})

Figure 3

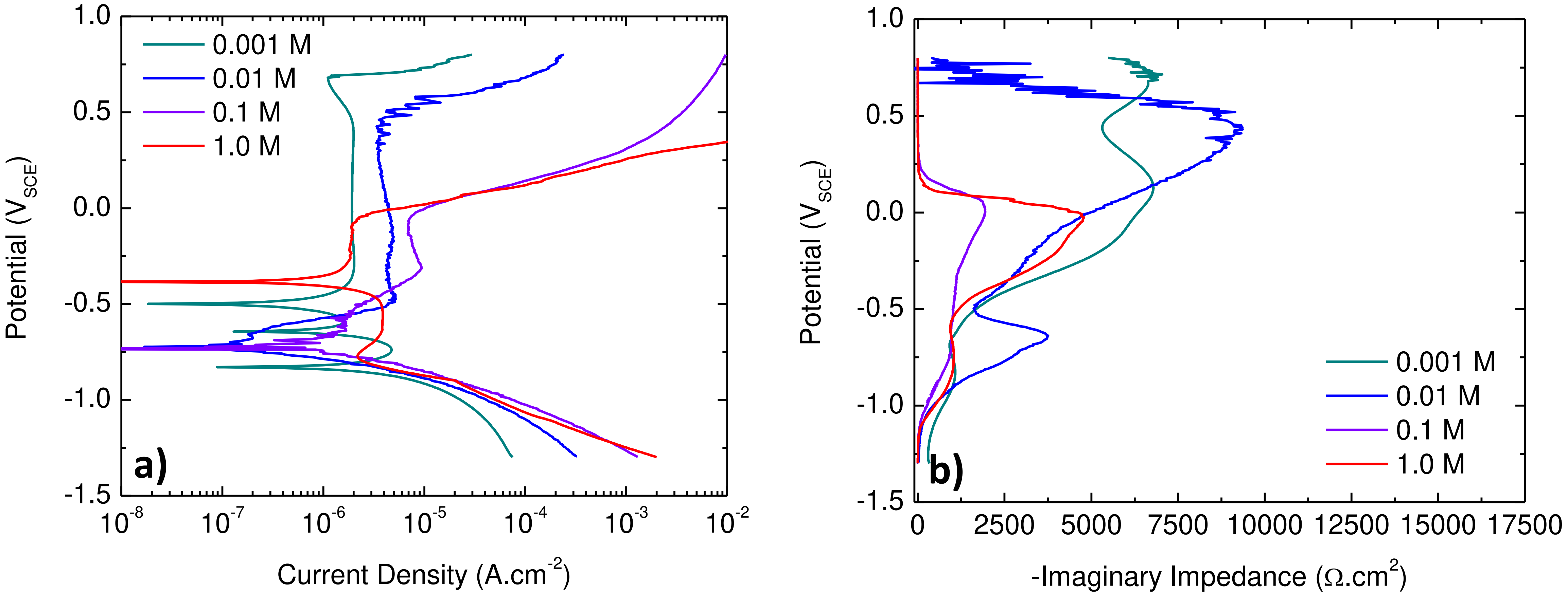

1.0
0.5
0.0
-0.5
-1.0
-1.5
Potential (V_{SCE})
0.001 M
0.01 M
0.1 M
1.0 M
a)
10^{-8}
10^{-7}
10^{-6}
10^{-5}
10^{-4}
10^{-3}
10^{-2}
Current Density (A.cm^{-2})
1.0
0.5
0.0
-0.5
-1.0
-1.5
Potential (V_{SCE})
0.001 M
0.01 M
0.1 M
1.0 M
b)
0
2500
5000
7500
10000
12500
15000
17500
-Imaginary Impedance (Ω.cm^2)

Figure 4

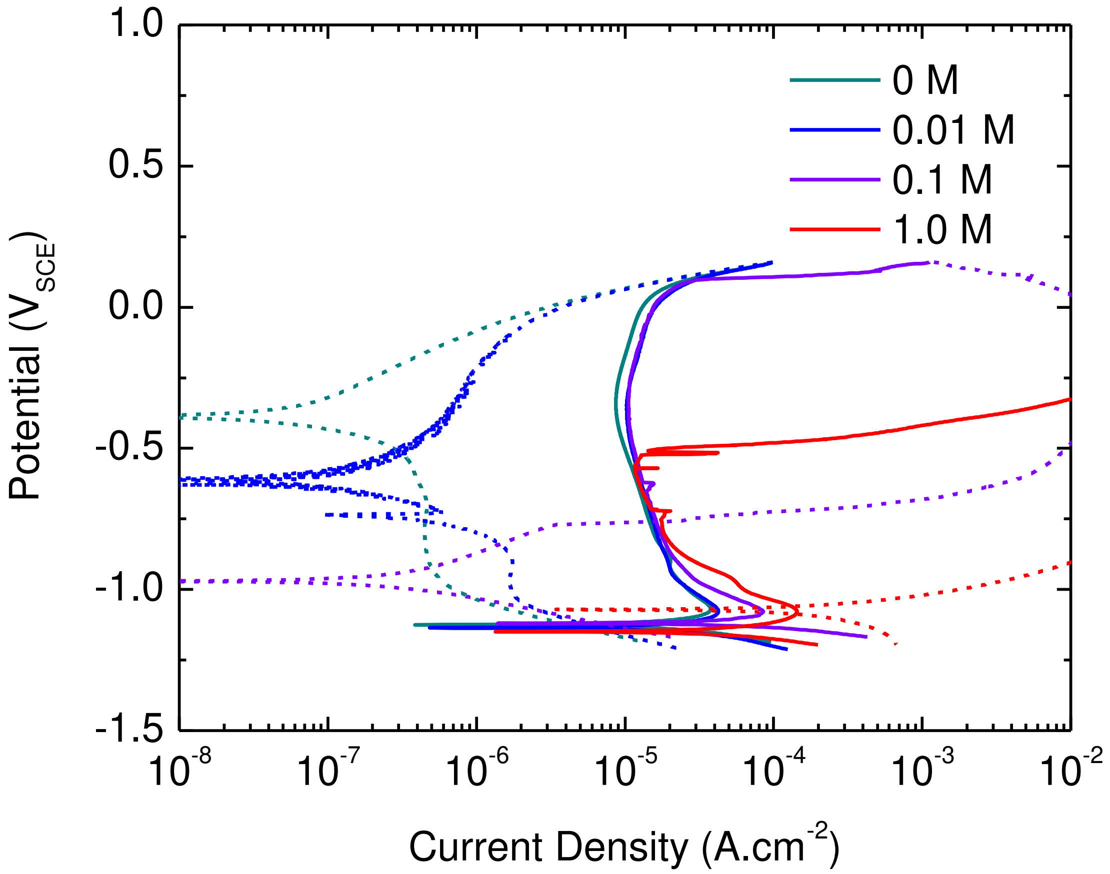
1.0
0.5
0.0
-0.5
-1.0
-1.5
Potential (V_{SCE})
10^{-8}
10^{-7}
10^{-6}
10^{-5}
10^{-4}
10^{-3}
10^{-2}
Current Density ($A.cm^{-2}$)
0 M
0.01 M
0.1 M
1.0 M

Figure 5

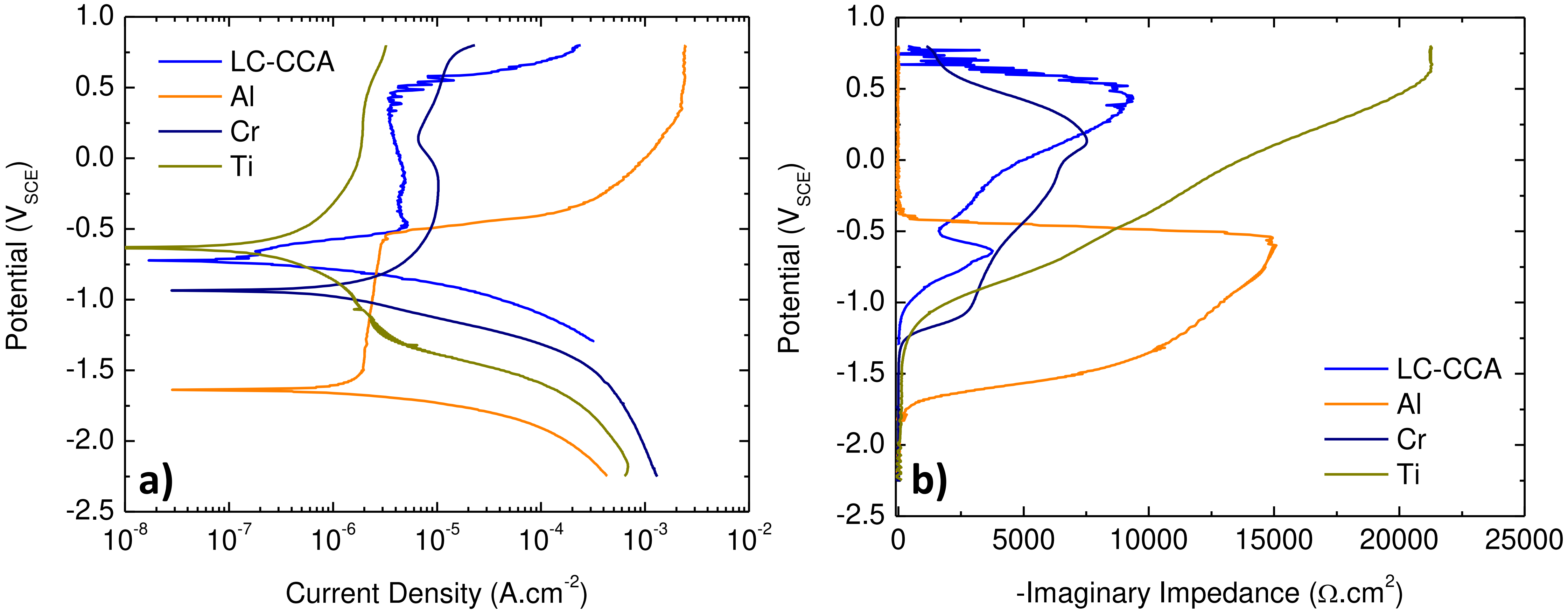
a)
Potential (V_{SCE})
Current Density ($A.cm^{-2}$)
1.0
0.5
0.0
-0.5
-1.0
-1.5
-2.0
-2.5
10^{-8}
10^{-7}
10^{-6}
10^{-5}
10^{-4}
10^{-3}
10^{-2}
LC-CCA
Al
Cr
Ti
b)
Potential (V_{SCE})
-Imaginary Impedance ($\Omega.cm^2$)
1.0
0.5
0.0
-0.5
-1.0
-1.5
-2.0
-2.5
0
5000
10000
15000
20000
25000
LC-CCA
Al
Cr
Ti

Figure 6

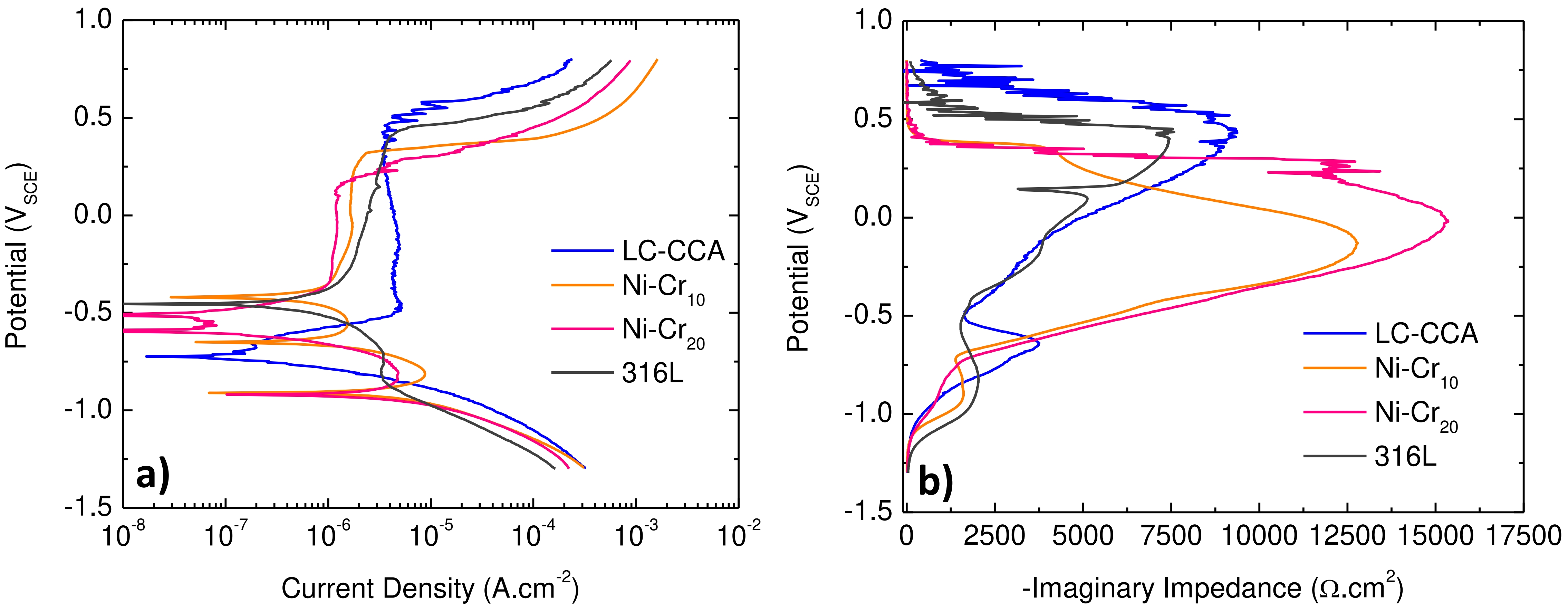
a)
Potential (V_{SCE})
1.0
0.5
0.0
-0.5
-1.0
-1.5
10^{-8}
10^{-7}
10^{-6}
10^{-5}
10^{-4}
10^{-3}
10^{-2}
Current Density ($A.cm^{-2}$)
LC-CCA
Ni-Cr_{10}
Ni-Cr_{20}
316L
b)
Potential (V_{SCE})
1.0
0.5
0.0
-0.5
-1.0
-1.5
0
2500
5000
7500
10000
12500
15000
17500
-Imaginary Impedance ($\Omega.cm^2$)
LC-CCA
Ni-Cr_{10}
Ni-Cr_{20}
316L

Figure 7: AESEC LSV

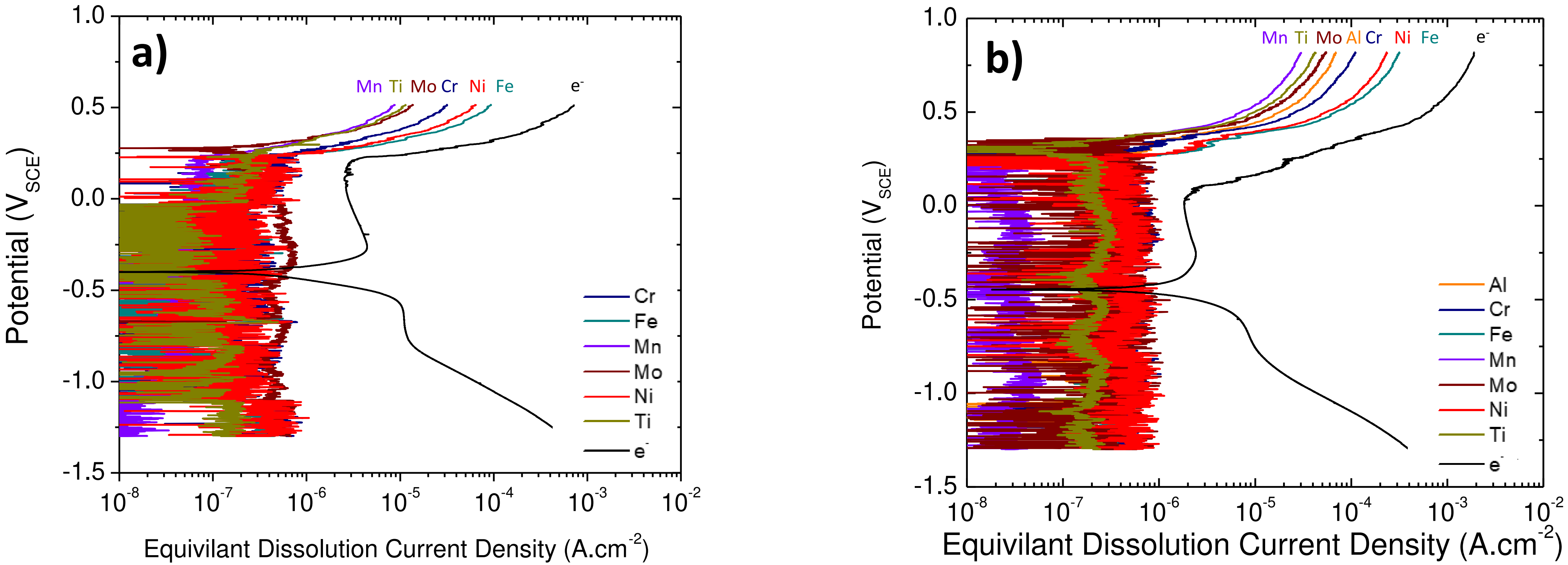

Figure 8

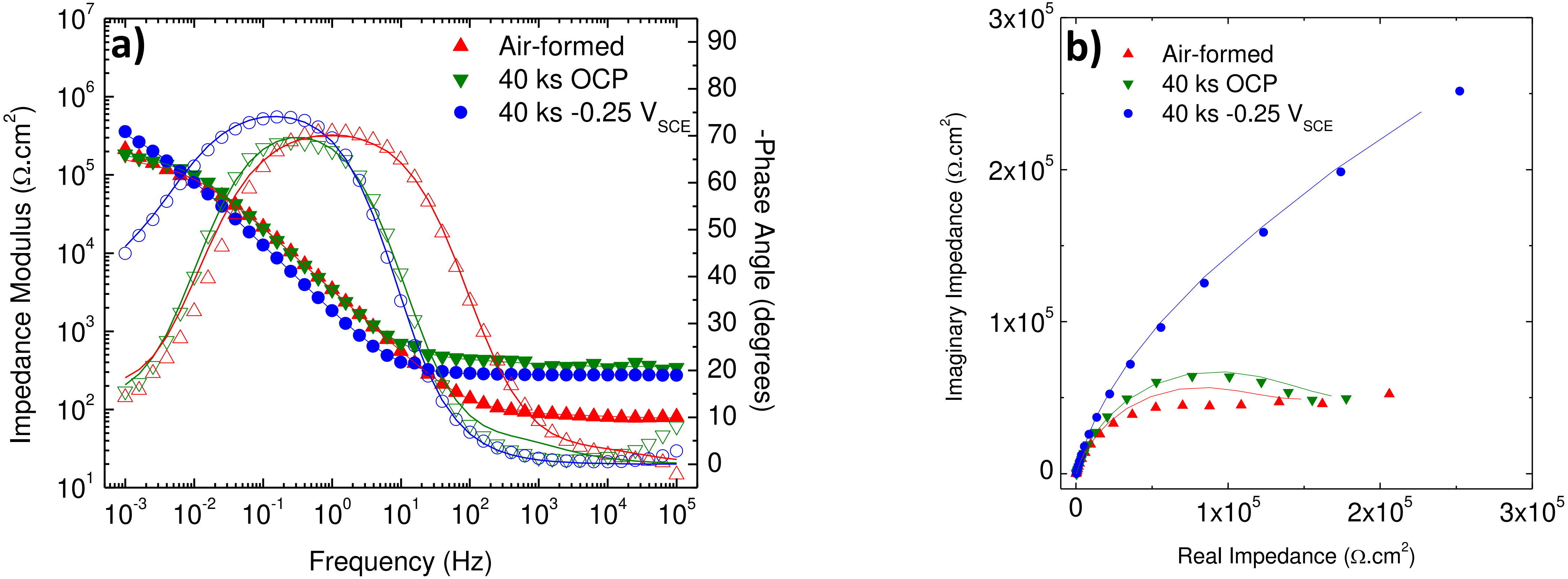

a)
Air-formed
40 ks OCP
40 ks -0.25 V$_{SCE}$
Impedance Modulus (Ω.cm^2)
10^7
10^6
10^5
10^4
10^3
10^2
10^1
-Phase Angle (degrees)
90
80
70
60
50
40
30
20
10
0
10^{-3}
10^{-2}
10^{-1}
10^0
10^1
10^2
10^3
10^4
10^5
Frequency (Hz)
b)
Air-formed
40 ks OCP
40 ks -0.25 V$_{SCE}$
Imaginary Impedance (Ω.cm^2)
$3x10^5$
$2x10^5$
$1x10^5$
0
Real Impedance (Ω.cm^2)
0
$1x10^5$
$2x10^5$
$3x10^5$

Figure 8 cont.

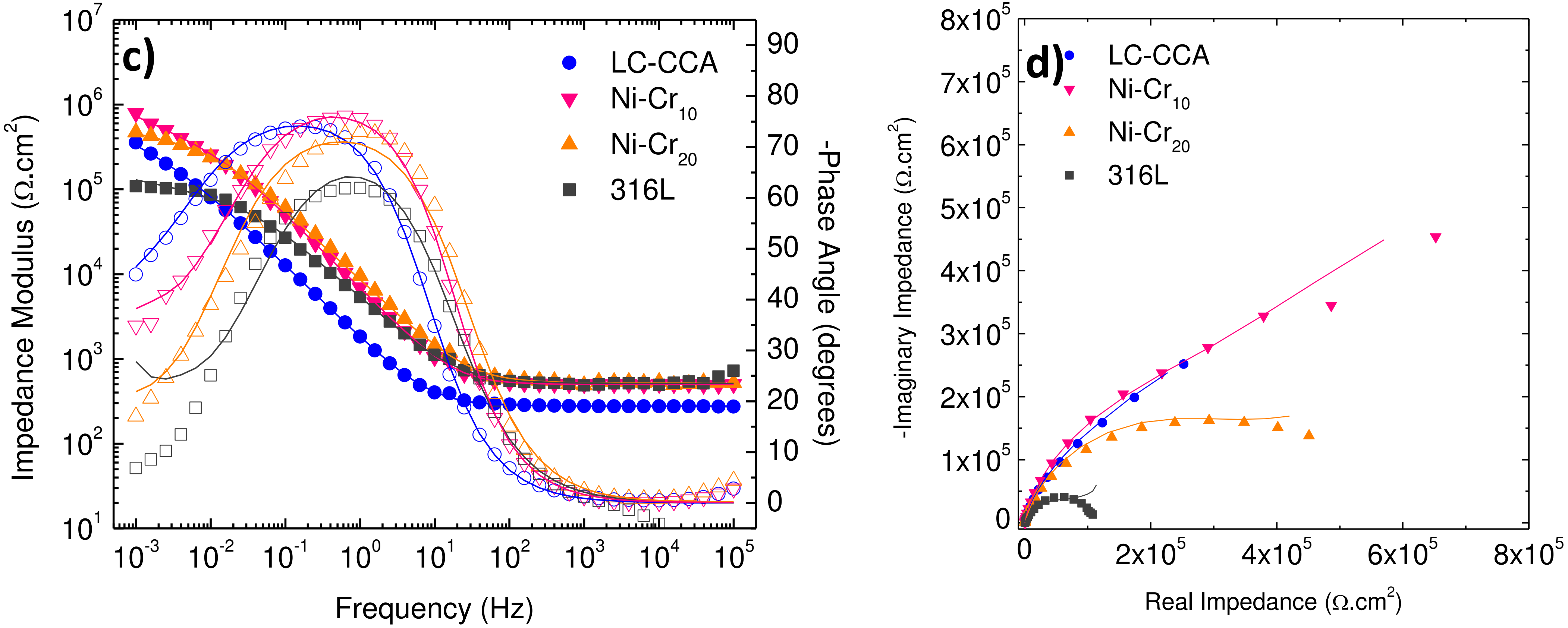

Figure 8 cont.

e)

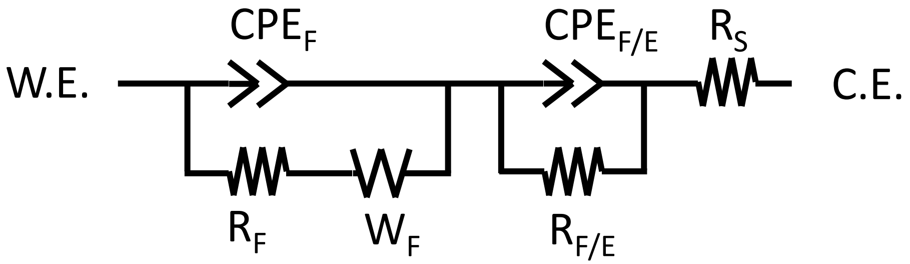

Figure 9

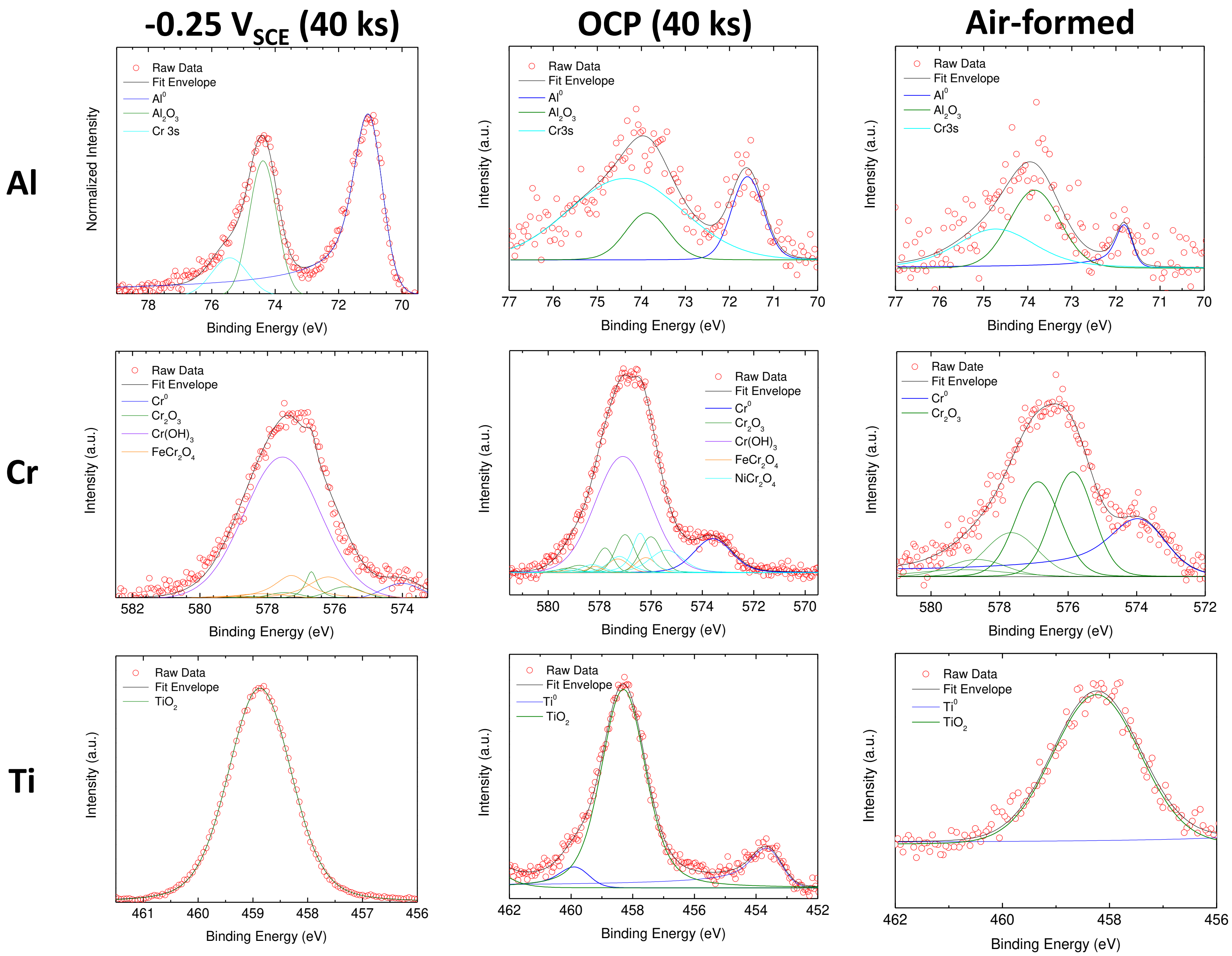
-0.25 V$_{SCE}$ (40 ks)
OCP (40 ks)
Air-formed
Al
Cr
Ti
Raw Data
Fit Envelope
Al^0
Al$_2$O$_3$
Cr 3s
Cr3s
Normalized Intensity
Intensity (a.u.)
Binding Energy (eV)
78
76
74
72
70
77
75
73
71
Cr^0
Cr$_2$O$_3$
Cr(OH)$_3$
FeCr$_2$O$_4$
NiCr$_2$O$_4$
Raw Date
582
580
578
576
574
572
570
TiO$_2$
Ti^0
461
460
459
458
457
456
462
454
452

Figure 10

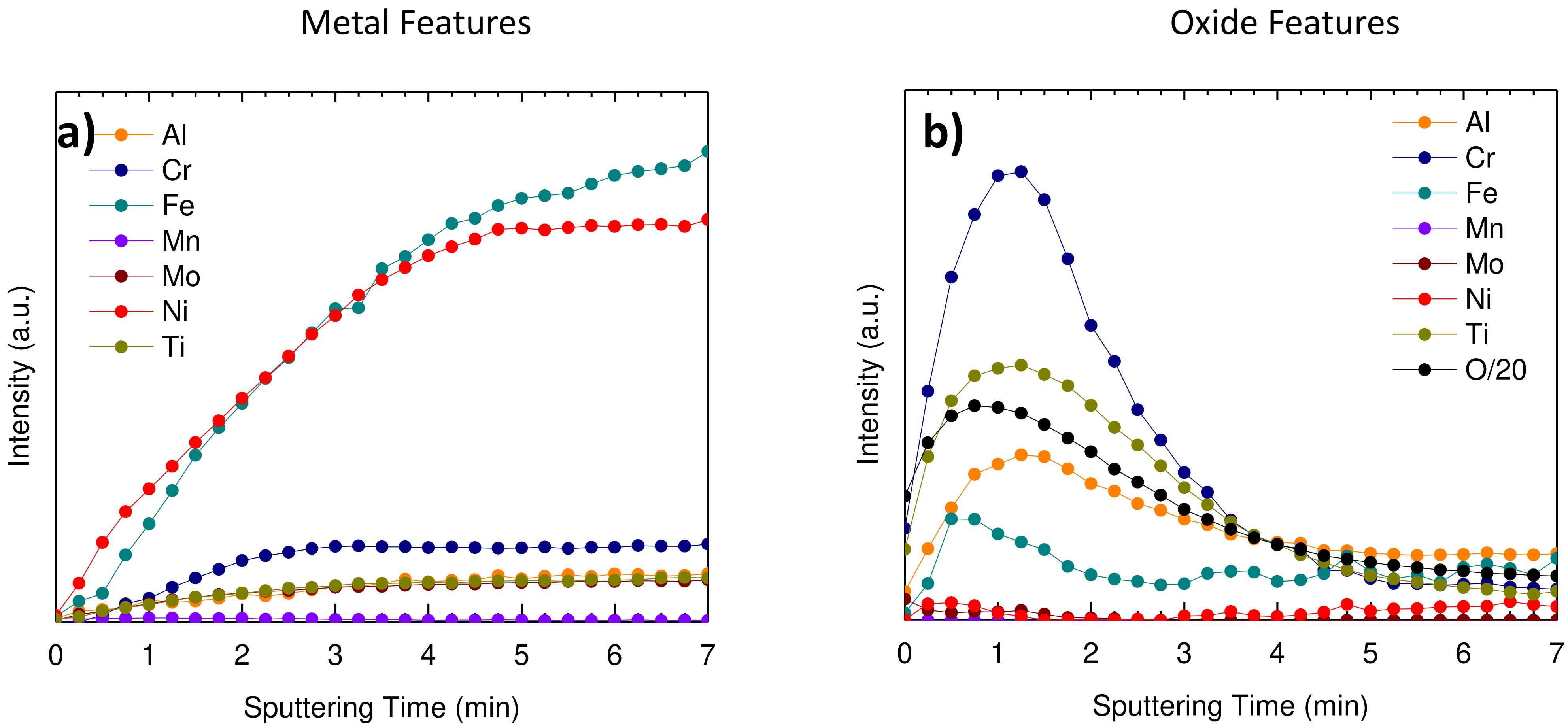

Metal Features

Oxide Features

Figure 11

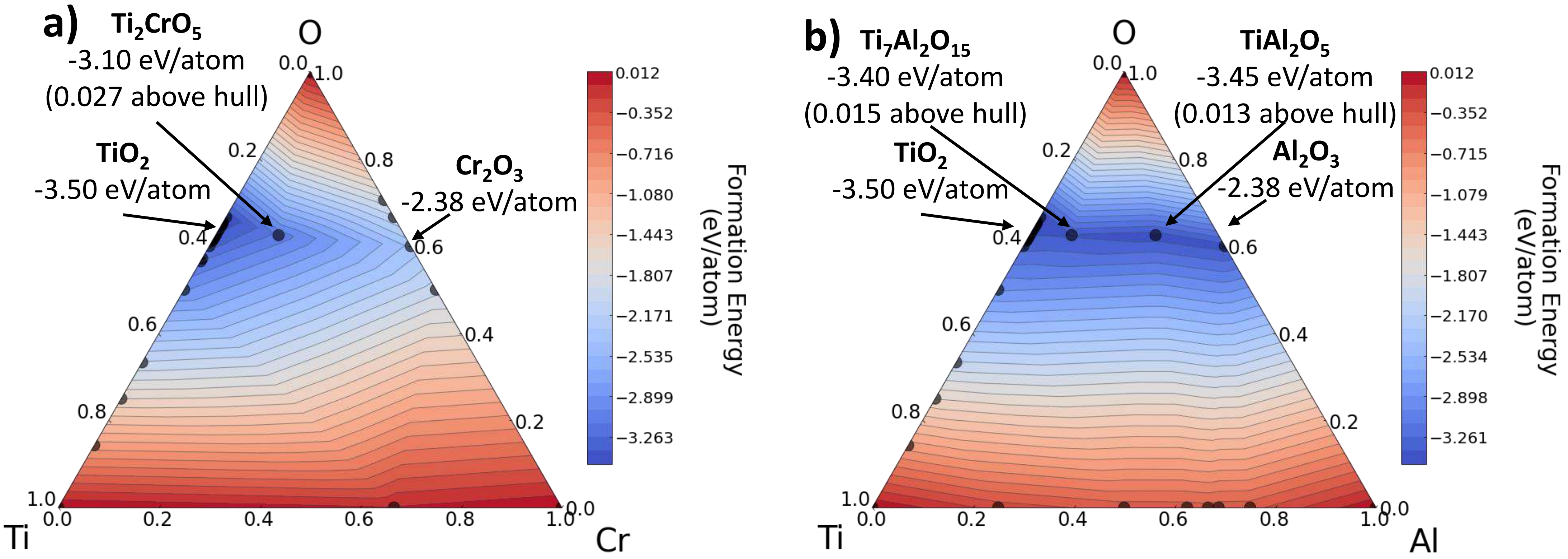

a) **Ti_2CrO_5** -3.10 eV/atom (0.027 above hull)

TiO_2 -3.50 eV/atom

Cr_2O_3 -2.38 eV/atom

b) **$Ti_7Al_2O_{15}$** -3.40 eV/atom (0.015 above hull)

TiO_2 -3.50 eV/atom

$TiAl_2O_5$ -3.45 eV/atom (0.013 above hull)

Al_2O_3 -2.38 eV/atom

Tables

Table I

Alloy	Al	Cr	Fe	Mn	Mo	Ni	Ti
LC-CCA	6.0%	10.0%	40.0%	5.0%	3.0%	30.0%	6.0%
Ni-Cr$_{10}$	0.0%	10.0%	0.0%	0.0%	0.0%	90.0%	0.0%
Ni-Cr$_{20}$	0.0%	20.0%	0.0%	0.0%	0.0%	80.0%	0.0%
316L	0.0%	18.3%	65.7%	2.1%	1.5%	11.4%	0.0%

Table II

Alloy	E_{Pit} (V_{SCE})	E_{Corr} (V_{SCE})	E_{Rep} (V_{SCE})	i_{Pass} ($\mu A.cm^{-2}$)
LC-CCA	0.574 ± 0.106	-0.768 ± 0.015	0.206 ± 0.107	3.44 ± 0.48
316L	0.407 ± 0.080	-0.461 ± 0.009	-0.003 ± 0.019	1.35 ± 0.31
Ni-10Cr	0.383 ± 0.219	-0.905 ± 0.005	-0.139 ± 0.033	1.36 ± 0.22
Ni-20Cr	0.291 ± 0.111	-0.921 ± 0.012	-0.118 ± 0.015	1.28 ± 0.17

Table III

Condition	R_f ($M\Omega.cm^2$)	$R_{f/e}$ ($\Omega.cm^2$)	R_s ($\Omega.cm^2$)	α_f	$\alpha_{f/e}$	Y_f ($\mu S.s^{\alpha}.cm^{-2}$)	$Y_{f/e}$ ($\mu S.s^{\alpha}.cm^{-2}$)	Y_W ($\mu S.s^{\alpha}.cm^{-2}$)	B_W ($s^{0.5}$)
Electrochemical Growth (-0.25 V_{SCE}, 40 ks)	264	0.18	277.2	0.862	0.752	117.0	37.0	42.6	38.8

OCP Exposure (40 ks)	161	66.09	353.4	0.836	0.753	67.1	30.7	325.5	37.2
Air-formed	139	8.35	77.1	0.810	0.754	66.6	30.7	304.6	39.6
Ni-10Cr (-0.25 V_{SCE}, 40 ks)	237	0.00	494.0	0.889	0.734	22.9	44.4	21.4	37.1
Ni-20Cr (-0.25 V_{SCE}, 40 ks)	362	3.84	512.6	0.835	0.670	25.4	44.2	71.4	31.4
316L (-0.25 V_{SCE}, 40 ks)	80	0.00	511.8	0.806	0.775	42.9	56.2	153.4	22.5

Table IV

Condition	R_f (MΩ.cm^2)	$R_{f/e}$ (Ω.cm^2)	R_s (Ω.cm^2)	α_f	$\alpha_{f/e}$	Y_f (µS.s$^{\alpha}$.cm^{-2})	$Y_{f/e}$ (µS.s$^{\alpha}$.cm^{-2})	Y_W (µS.s$^{\alpha}$.cm^{-2})	B_W (s$^{0.5}$)
Electrochemical Growth (-0.25 V_{SCE}, 40 ks)	264	0.18	277.2	0.862	0.752	117.0	37.0	42.6	38.8
OCP Exposure (40 ks)	161	66.09	353.4	0.836	0.753	67.1	30.7	325.5	37.2
Air-formed	139	8.35	77.1	0.810	0.754	66.6	30.7	304.6	39.6
Ni-10Cr (-0.25 V_{SCE}, 40 ks)	237	0.00	494.0	0.889	0.734	22.9	44.4	21.4	37.1
Ni-20Cr (-0.25 V_{SCE}, 40 ks)	362	3.84	512.6	0.835	0.670	25.4	44.2	71.4	31.4
316L (-0.25 V_{SCE}, 40 ks)	80	0.00	511.8	0.806	0.775	42.9	56.2	153.4	22.5

Table V

Alloy	LC-CCA	316L
ASTM G-48-A (mg.cm^{-2}.y^{-1})	9790	3900
0.1 M NaCl pH 4 (mg.cm^{-2}.y^{-1})	5.894	0.833
0.1 M NaCl pH ~5.75 (mg.cm^{-2}.y^{-1}) [61]	Trace	Trace

Table VI

Growth Condition	Al	Cr	Fe	Mn	Mo	Ni	Ti
X''^{S}: Kirhkheim Model (-0.25 V_{SCE} dissolution rates)	0.008	**2.367**	0.003	0.001	**1.046**	**1.381**	**5.262**
Electrochemical Growth (-0.25 V_{SCE}, 40 ks)	**2.75**	**1.43**	0.23	0.02	0.77	0.08	**9.23**
OCP Exposure (40 ks)	0.60	**4.61**	0.10	0.06	**5.03**	0.30	**3.61**
Air-formed	**1.95**	**2.65**	0.72	0.30	**2.77**	0.09	**3.38**